BACHELOR' S THESIS / BIOMEDICAL ENGINEERING 2022

Beyond exponential fitting: a Deep Learning approach for accurate and robust T1 estimation from Cardiac Magnetic Resonance MOLLI sequences

Pau Altur Pastor

upf. Universitat Pompeu Fabra Barcelona

Beyond exponential fitting: a Deep Learning approach for accurate and robust T1 estimation from Cardiac Magnetic Resonance MOLLI sequences

Pau Altur Pastor

Bachelor's thesis UPF 2021/2022

Thesis supervisor:

Dr. Gaspar Delso (GE Healthcare)

UPF tutor:

Pr. Oscar Camara

Dedicatory

To Paula, who sees it clear even when I do not.

Acknowledgments

I would like to start by thanking my supervisors Dr. Gaspar Delso and Pr. Oscar Camara for their invaluable help during the realization of this bachelor's thesis. I am especially grateful to Dr. Delso for patiently imparting his knowledge of Cardiac Magnetic Resonance to me and guiding me through this often challenging but also very rewarding project. Such dedication is made all the more generous by the fact that he has no teaching obligations toward Biomedical Engineering undergraduates at Universitat Pompeu Fabra, and still, he chooses to offer projects and share his experience with those who want to dive into the world of Cardiac Magnetic Resonance. I would also like to thank Maria Ángeles Iglesias for sharing her work on the estimation of T1 using DeepBLESS, which laid the foundations for this project.

Both Hospital Clínic and GE Healthcare have also played an integral role in this thesis. All of the clinical data employed in this work has been acquired at Hospital Clínic as part of their research collaboration with GE Healthcare on Cardiac Magnetic Resonance. Since I have thanked the hospital, I would be remiss not to thank Dr. Adelina Doltra and Santi Sotes for kindly showing me around the CMR unit at Hospital Clínic and offering me a fresh new perspective on medical imaging from a clinical point of view.

Finally, on a personal level, I would like to thank my family, friends, and partner for accompanying me on this journey. Only my parents and siblings know how many dinner table conversations I have hijacked with updates about the progress of my thesis or the umpteenth explanation of how Magnetic Resonance Imaging works. In a similar vein, my girlfriend Paula has been by my side and encouraged me to carry on even when I thought it was hopeless to keep trying.

Abstract

T1 parametric maps of the myocardium are a recent development in cardiac Magnetic Resonance Imaging (MRI). They can be used to characterize the composition of the heart and identify alterations that can be indicative of a pathology. A common method of T1 estimation involves pixel-wise non-linear curve fitting from Modified Look-Locker Inversion Recovery (MOLLI) series. Whilst relatively accurate, this method presents several drawbacks. Firstly, it assumes magnetization recovery to be a purely exponential process dependent on T1, thus neglecting other parameters such as T2 and B1 that can interfere in the process. Secondly, it does not consider that each acquisition during an inversion recovery experiment inverts the magnetization vector by a given angle and thus delays the recovery. Finally, since it considers each pixel individually, neglecting spatial information, it is sensitive to image quality. Additionally, since non-linear curve fitting is an iterative algorithm, it is computationally expensive and time-consuming. To address these issues a convolutional neural network, DeepBLESS, and two spatially-aware variants of it, were trained to predict T1, T2, and B1 with a dataset of MOLLI series simulated from experimental data. The simulation was performed using Bloch simulations. Thus, a dataset could be generated without relying on exponential fitting for ground truth generation. It was shown that the Deep Learning approaches eliminated the underestimation bias of exponential fitting with the spatially-aware network Median-DeepBLESS being more robust to noise than both exponential fitting and the standard DeepBLESS network for myocardial T1 estimation. Accurate estimation of T2 and B1 from MOLLI sequences was also accomplished through the Deep Learning approach, which may lead to simultaneous T1, T2, and B1 estimation in common clinical practice in the future.

Keywords

Cardiac Magnetic Resonance, T1 estimation, Modified Look-Locker Inversion Recovery, Deep Learning, Bloch equations

Preface or prologue

The current project is born out of a curiosity about how artificial intelligence can impact healthcare and produce tangible improvements in people's lives. During the four years of my Biomedical Engineering degree, I have progressively felt more and more interested in the topic of Machine and Deep Learning applied to clinical settings. Deep Learning especially seems to me like a very elegant way of approaching many problems. You just need sufficient data, of sufficient quality, and the algorithm does the rest, often with spectacular performance.

If there is one field of medicine where the application of AI has been transformative it is medical imaging. Every year more and more articles are published on new algorithms that outperform experts in every task, from segmentation to diagnosis. This has led some to predict that clinicians will be replaced by robots in the near future. I am not sure about that, but I firmly believe that AI tools have great potential in aiding radiologists and improving the standard of care for patients worldwide.

One of the specialties that relies the most on imaging is cardiology. Magnetic Resonance is of especially great use to cardiologists, since the heart is composed of soft tissue, and alterations in it can be indicative of underlying disease. Thus, accurate MRI of the heart is crucial for the diagnosis and treatment of many patients with pathologies that could be potentially lethal if undetected. Lately, there has been a push towards quantitative measures of the heart's physiology, anatomy, and function, to improve diagnostic performance in cases where distinguishing among pathologies might be difficult. T1 mapping is one of those quantitative approaches. It allows to characterize the magnetic properties of the myocardium and compare them with reference values to quantify potential differences.

Myocardial T1 mapping was first introduced around the turn of the century. Due to the particular characteristics of the heart (beating, close to the lungs), estimating T1 maps of it is not straightforward. Several different acquisition schemes have been proposed, but the one that has become widespread in clinical practice is Modified Look-Locker Inversion-Recovery (MOLLI). Although it offers great reproducibility and signal-to-noise ratio, this approach presents one main drawback which is its bias when estimating T1 and its sensitivity to confounders such as variations in T2 or flip angle. To address these issues, several approaches have been proposed, such as the one presented in this project which employs Deep Learning to correct the systematic estimation errors that happen when estimating T1.

Index

Page

List of figures

Page

List of tables

Page

1. INTRODUCTION

Magnetic Resonance Imaging (MRI) has revolutionized diagnostic medicine since its introduction in 1977, more than 40 years ago (1). It is an imaging modality that leverages fundamental physical properties of tissues to allow the exploration of human internal organs in a non-invasive way. Since it does not rely on attenuation to acquire an image, unlike X-Ray based imaging modalities, it offers unparalleled soft tissue contrast (2). Thus, it is useful when evaluating alterations in specific soft tissues that could be indicative of a disease, such as a scar left by a myocardial infarct (3) or plaques in the central nervous system that signal a multiple sclerosis relapse (4).

MRI works by probing the magnetic properties of the tissues that are scanned. To do so, it takes advantage of the coil-like properties of the hydrogen atom. Thus, under the influence of a large magnetic field, the nuclear magnetization of the atoms aligns itself with the direction of the main magnetic field (B0), with a precession around it. However, when excited with a radiofrequency pulse (B1) of the same frequency as its precession (resonant), the net magnetization vector (NMV) of a tissue containing hydrogen atoms, can be nutated by a given angle (up to 180º). Upon ceasing this pulse, the NMV will recover to its steady-state in the direction of the main magnetic field, releasing RF energy into its surroundings. Such recovery is determined by two main components, longitudinal (T1) and transverse (T2) relaxation, and the RF it releases can be detected (5). For detailed explanations of MRI terms see the Alphabetical Index at the end of this document.

Longitudinal, or T1 relaxation, is due to the energy exchange between the spin of each H-atom and the surrounding lattice (6). It follows an exponential curve,

$$M_t = M_{max}\left(1 - e^{-\frac{t}{T1}}\right), \quad (1)$$

and it is characterized by the T1 time constant which is the amount of time it takes the longitudinal magnetization to return to a fraction e^{-1} of its steady-state value. The specific value of the T1 constant of a given tissue is dependent on magnetic field strength. The larger the field strength the longer T1 values are (7).

Transverse, or T2 relaxation, is the result of spin dephasing. As spins recover, they interact with each other, modifying their precession rate in a temporary and random manner. Thus, transverse magnetization is progressively lost until almost disappearing (8). In the same way that T1, T2 relaxation also follows an exponential curve,

$$M_t = M_{max}\left(1 - e^{-\frac{t}{T2}}\right), \quad (2)$$

characterized by the time constant T2 which is the amount of time it takes the transverse magnetization to return to a fraction e^{-1} of its steady-state value. T2 values are unrelated to magnetic field strength (9).

1.1 Myocardial T1 mapping

Rapid innovations in cardiovascular magnetic resonance (CMR) have allowed the routine acquisition of quantitative measures of T1 in the myocardium and blood (10). Such quantification requires the acquisition of multiple images at different points of the recovery curve to estimate the exponential time constant for MR longitudinal relaxation, T1 (11). Then, this parameter can be displayed pixel-wise in a so-called "T1 map", where an estimate of T1 is encoded in the intensity of each pixel (12,13).

Because of its quantitative character, standard T1 ranges may be established, and colors can be allocated to T1 values to make visual understanding easier (see Figure 1 for an example). This possibility opened a new era in cardiology, allowing practitioners and researchers to measure physiologically significant features of both the regional and global myocardium, regardless of function. Diffuse myocardial disease has traditionally been difficult to assess or even recognize noninvasively. This breakthrough is significant because focal and diffuse alterations may directly represent pathophysiologic processes throughout the illness spectrum, from preclinical to end-stage disease (10).

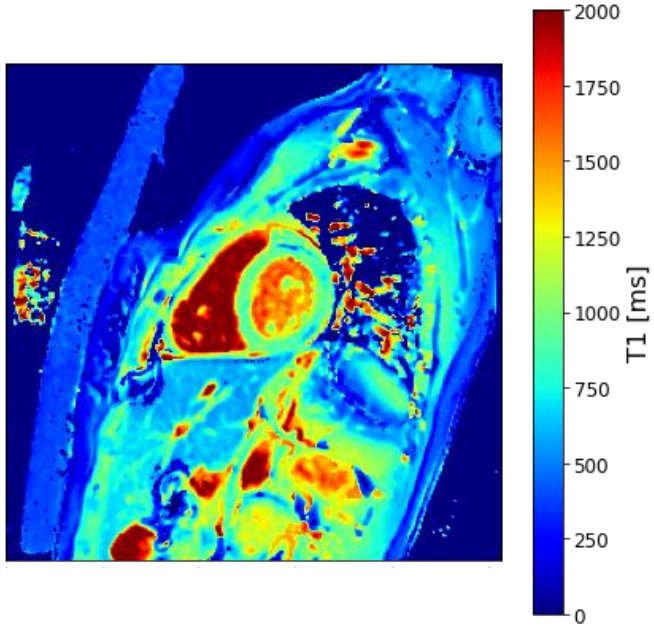

Figure 1: T1 map estimated from clinically acquired Magnetic Resonance Imaging sequence. Pixel color in the image indicates the T1 value in ms. Large T1 values (red) correspond to blood whereas medium values (yellow, green) correspond to the myocardium and other soft tissues and low T1 values (blue) correspond mostly to air.

CMR is able to track biologically important changes in the myocardium using either: a) native (non-contrast) T1, which reflects myocardial disease involving the myocyte and interstitium without the use of gadolinium-based contrast agents (GBCA); or b) the extracellular volume fraction (ECV) after administering a GBCA, a direct measurement of the magnitude of the extracellular space, which may reflect interstitial disease. The latter technique attempts to dichotomize the myocardium into its cellular and interstitial components with estimates expressed as volume fractions. The concept of employing extracellular agents to quantify the interstitial space has been exploited by investigators over many decades. Advances in T1 measurement now permit routine non-invasive measurement of ECV (14–17).

a) Clinical practice

T1 maps are not specific and so reflect changes in the composition of tissues. Native T1 is mainly influenced by the water, protein, lipid, and iron content of the tissue it belongs to and expresses a signal from the intracellular and extracellular compartments. On the other hand, postcontrast T1 is shorter than native T1 and is mainly informative about the extracellular compartments. That is why it is used to calculate ECV (18).

ECV is a measure of the amount of space, which is unoccupied by cells, and it includes the plasma volume within the capillaries. It shows a correlation with the volume fraction of collagen, but it also increases when there is amyloid or myocardial edema. In the absence of such edema and other forms of infiltrative disease, ECV can be seen as a biomarker for interstitial disease or myocardial fibrosis (19).

T1 alteration can be diagnostically relevant, both when increased (12,20–25) or decreased (26–30). As seen in Figure 2, the level of alteration of both Native T1 and ECV is a diagnostic marker of several myocardial pathologies, and it can be used to discriminate among them.

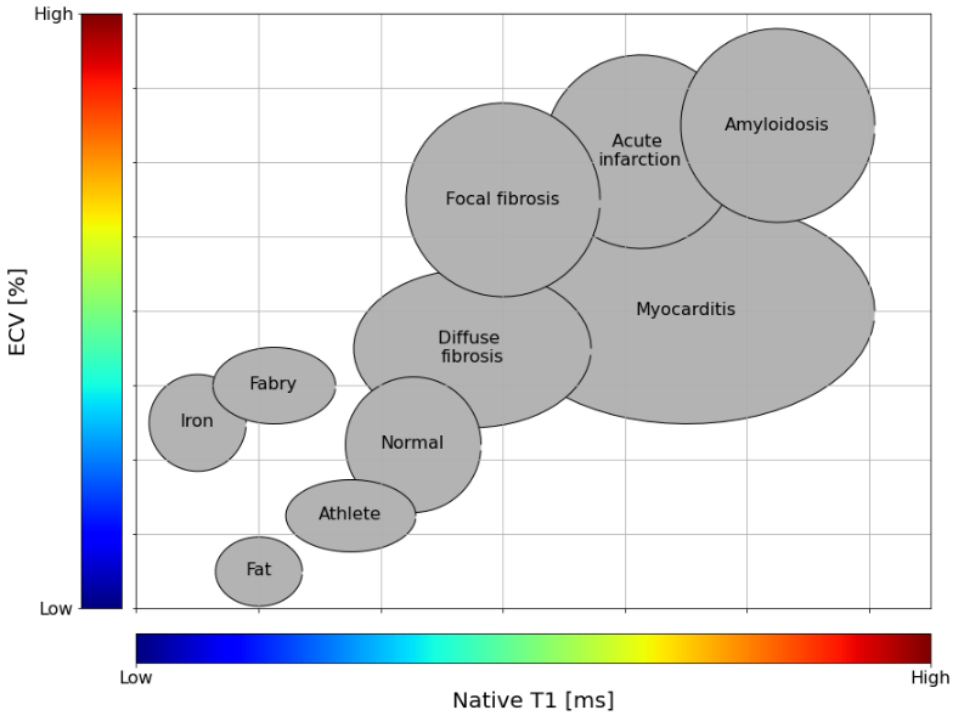

Figure 2: Relationship between altered T1 and ECV values, and myocardial disease. Adapted from Martin Ugander (SCMR, 2014).

b) Acquisition methods

T1 maps are estimated from several different images acquired with different T1 weightings. The signal intensities are then fitted to the equation for T1 relaxation to estimate T1. To accurately estimate T1 using a three-parameter curve-fitting approach, data from at least 6 to 10 different inversion time points should be available (31). This is an obstacle since one must consider that patients must hold their breath during acquisition

to reduce movement artifacts and have all acquired images within the same frame of reference (13). Although myocardial T1 values are relatively short, around 1150 ms at 3 T (32), each magnetization recovery experiment requires a relaxation period of 4 to 5 times the T1 (33) to allow for full magnetization recovery after each inversion pulse. That means that only four to five measurements can be performed within a single breath-hold (20 s). The recovery experiments can be initiated with a 180º inversion pulse (13,34) or a 90º saturation pulse (35,36). Saturation recovery (SR) techniques are more accurate than inversion recovery (IR) techniques, but the latter are more reproducible due to their larger dynamic range (11), which is the reason why they are the preferred method in clinical practice (37). The focus of the current project will be on inversion recovery techniques.

LOOK-LOCKER

To circumvent the limitation on the number of measurements that can be performed within a single magnetization recovery experiment, a multi-point approach was proposed by Look and Locker in the 1970s (38). It consists of sampling the relaxation curve at multiple time points after a 180º degree pulse (39). Samples from different IR measurements are then ordered and T1 is estimated using pixel-wise exponential fitting. This method is widely used in T1 mappings of the brain (40–43). Nevertheless, it is not suitable for pixel-by-pixel T1 mapping of the heart due to its disregard for cardiac motion. That means that T1 values can only be calculated for manually defined regions of interest, which is not practical in clinical practice and can lead to inaccuracy due to misregistration effects (15).

MODIFIED LOOK-LOCKER INVERSION RECOVERY

A proposed method to obtain multi-point measurements from IR experiments in a way that takes heart motion into account and allows for automated estimation of T1 values without the need for manual intervention is through Modified Look-Locker Inversion Recovery (MOLLI) sequences (see Figure 3) (13).

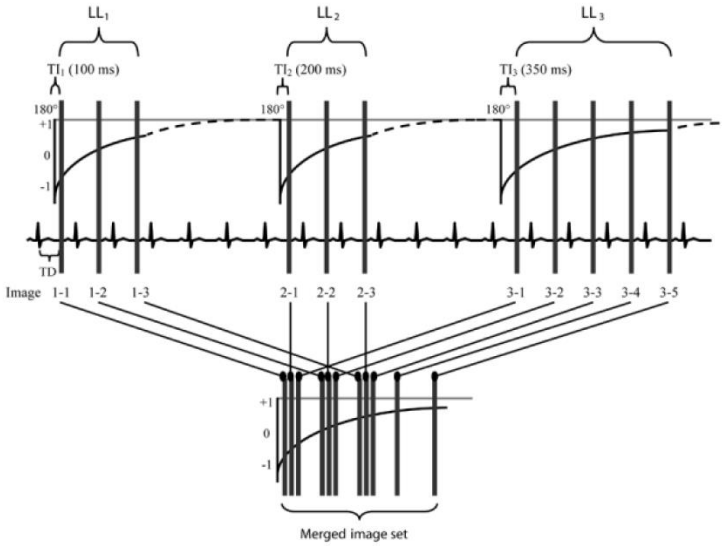

Figure 3: Diagram depicting the way in which MOLLI series combine samples from several IR experiments to compose a single curve from where to estimate T1. Vertical bars represent image acquisition. Dashed lines represent undisturbed magnetization recovery. Extracted from Messroghli et al. (13).

MOLLI sequences perform selective data acquisition at end-diastole over successive heartbeats (44) and merge the image set of several Look-Locker experiments with varying inversion times (TI) into a single data set. That way every image of the heart is in the same frame of reference. Although sampling in this way limits the number of images acquired to one per heartbeat, the use of multiple LL experiments with different TIs yields enough samples of the relaxation curve to accurately estimate T1.

There exist several different protocols for MOLLI acquisition that essentially vary on the number of Inversion Recovery experiments performed and the number of slices acquired in each inversion recovery experiment. The original protocol introduced by Messroghli et al. (13) utilized a 3(4s)3(4s)5 pulse scheme as seen in Figure 3, where three Look-Locker experiments were performed with 4 seconds of unperturbed recovery time between them. However, this scheme presents two main problems: first, it is very long and may present problems to maintain a breath-hold; and second, the use of three inversions of the NMV causes the second and especially the third experiment to be influenced by the previous ones. That is the reason for the popularization of shorter sequences such as the 5(3s)3 sequence (45) used to acquire the images employed in the current study.

A balanced steady-state free precession readout is chosen over a conventional Gradient-Echo readout due to its superior signal-to-noise ratio and its lower tendency to modulate the relaxation (46). The image data acquisition window is restricted to under 200 ms in end-diastole using sensitivity encoding (SENSE/ASSET) (47) with a reduction factor of 2, to minimize artifacts from cardiac motion.

LIMITATIONS

Although MOLLI sequences and non-linear exponential fitting are currently used in clinical practice to obtain T1 maps of the myocardium, they present some sub-optimal aspects that can be improved upon with current advances in Deep Learning (DL) algorithms applied to image processing.

Firstly, pixel-wise fitting to estimate T1 generally ignores spatial information as it only incorporates data from each pixel to calculate its T1 value (11), since incorporating a regularization term would add a significant computational cost. This, in turn, renders the estimation more susceptible to noise. Intuitively, one might expect a pixel's intensity to be similar to its surrounding pixels except when near a very abrupt edge. A pixel that is very different from all its neighbors is likely the product of noise and it can have a negative effect on the accuracy of T1 estimation.

Secondly, iterative methods such as the Levenberg-Marquardt algorithm have been traditionally used to estimate T1. Such algorithms are computationally expensive (48), something which translates into lengthy estimation times that have a significant impact on patient throughput in a clinical setting. With the current drive towards increased resolution in MRI (49), the computational cost of these methods grows quadratically with resolution. By contrast, DL models, although computationally expensive to train, are quite fast with forward passes of data (50).

Finally, a significant portion of the inaccuracy of exponential fitting for T1 estimation comes from the assumptions made about magnetization recovery (51). When estimating T1 in this way, the main underlying assumption is that the magnetization recovery

captured in the MOLLI series perfectly reflects the longitudinal relaxation of the NMV. However, this is not true since other factors also influence the magnetization that is measured through CMR.

It has been shown that the MOLLI method underestimates high T1 values with a relative error of more than 15% for values above 1500 ms (52). This is due to the fact that MOLLI combines both modulated and unmodulated magnetization recovery across several magnetization recovery experiments. Different approaches have been proposed to correct the bias caused by this effect (53–56). Nevertheless, variations in other parameters such as T2, nominal flip angle, or inversion efficiency also have a significant impact on the accuracy of T1 quantification (57). The main cause for inaccuracy in flip angle and inversion efficiency are inhomogeneities in the B1 field (58). These are caused by the off-center positioning of the patient's torso within the transmitting whole-body radiofrequency (RF) birdcage coil giving rise to unequal loading effects, and by a standing RF wave effect accentuated by the short RF quarter wavelength at 3T. Both effects are more pronounced at higher field strengths (59,60)

1.2 State of the art

To address the issues that exponential fitting for T1 estimation presents, several new approaches have been proposed to improve the accuracy of the standard three-parameter exponential fitting. An example of this is BLESSPC or Bloch Equation Simulation with Slice Profile Correction (53). As its name implies it is a method to simulate T1 relaxation using Bloch equations and estimate T1 through the numerical fitting of those equations. It achieved significant performance improvement over the standard fitting method, but it is very computationally costly and difficult to implement in clinical practice.

Because of the problems with traditional numerical approaches, one of the most promising avenues for improvement in this field is the use of DL algorithms to perform the estimation. That is thanks to these algorithms' ability to learn complex functions and consider the influence of multiple confounding factors (61). DL neural networks are algorithms loosely inspired by the computational logic of the human brain. Their basic unit is a perceptron (62) which is similar to a biological neuron. It takes in a linear weighted combination of its inputs, applies an activation function to it, and outputs a numerical value. Artificial neurons are organized into layers that flow unidirectionally from input to output. Deep Artificial Neural Networks are formed by numerous so-called hidden layers between the layer that receives the input and the one that produces the output. Such networks can be iteratively trained on labeled datasets to improve their performance at a given task as measured by a specific metric (63). The update of the weights of the network is done through a process called backpropagation, where the loss, defined as a function that measures the difference between predicted and expected outputs, informs how weights should be updated to improve model performance (64).

Convolutional Neural Networks (CNNs) are a subset of Artificial Neural Networks that cluster their weights into convolutional kernels of a given size, usually smaller than the input. These kernels slide across the input data and produce multiple outputs that are processed by other convolutional kernels downstream (65). The benefit of this approach is that it promotes shift-invariance and prevents overfitting since a single kernel is used on the whole input data instead of a neuron only receiving a specific part of the input (66).

That is why CNNs have been widely used in image analysis and time series problems with spectacular results (67–71).

Recently, Shao et al. (72) developed Deep Learning Bloch Equation Simulations (DeepBLESS, see Figure 4) to perform fast and accurate estimation of myocardial T1 and T2 values. This network, a CNN incorporating Resnet blocks, was trained on simulated radial T1-T2 and MOLLI sequences. It was then compared with the BLESSPC estimation approach (73) in simulation, phantom, and in vivo studies for the MOLLI sequence at 1.5 T and the radial T1-T2 sequence at 3T. DeepBLESS (Figure 4) showed comparable performance to BLESSPC when estimating T1 from MOLLI sequences but generated an entire map much faster.

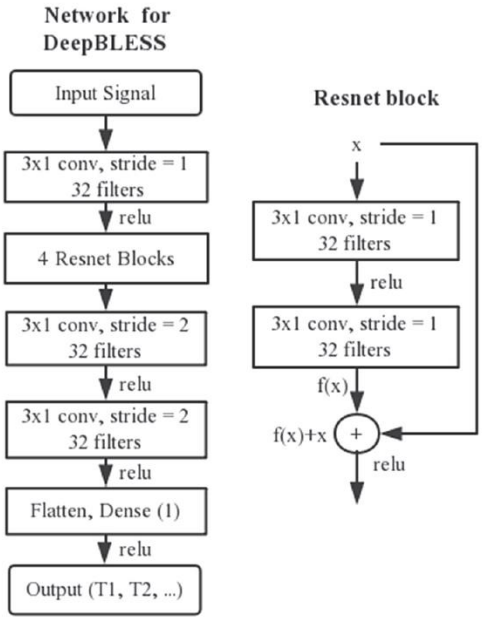

Figure 4: The architecture of the DeepBLESS neural network. Extracted from Shao et al. (72).

Additionally, DeepBLESS has also been explored as a means of incorporating spatial information into the T1 estimation process (74). A variant of the DeepBLESS algorithm was developed that incorporated information of the neighborhood of each pixel, in the form of its median, as input for the estimation. Thus, it was shown that this approach yielded a T1 estimation much more resilient to noise, as can be seen in Figure 5, whilst remaining significantly faster to generate than the traditional fitting pipeline.

Nevertheless, all of these DL approaches use traditional estimation through exponential fitting as their ground truth. As such, their performance will, at best, be the same as that of exponential fitting, and it will display the same biases when estimating T1 and the same sensitivity to variations in T2 and flip angle uncertainty.

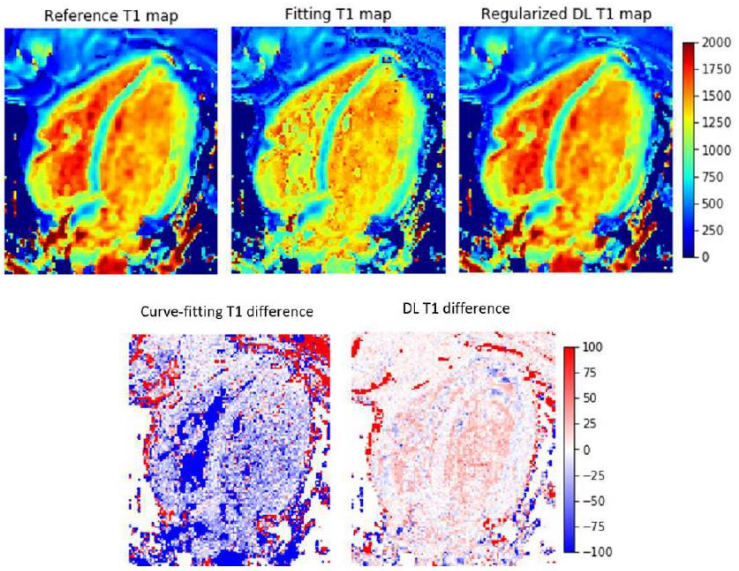

Figure 5: The reference, exponentially fitted and regularized DL T1 map, and the estimation difference between reference and fitted T1 map, and reference and regularized DL T1 map. Extracted from Iglesias et al. (74).

1.3 Objectives

The four main objectives of the current project were the following:

1. Test whether numerical simulation of MOLLI series with Bloch equations allows building a dataset that accurately captures the magnetization recovery curve and can be used to train algorithms to accurately estimate T1 in the presence of confounders.

2. Develop a pipeline based on the DeepBLESS architecture that can accurately estimate T1 from simulated MOLLI series with less bias than traditional fitting approaches.

3. Test whether the developed pipeline can uncouple T1 from other factors that influence magnetization recovery, namely T2 and field inhomogeneities in B1. Ideally, it should be able to approximately estimate the value of T2 and B1 along with T1.

4. Increase the robustness of the developed pipeline by incorporating spatially-aware strategies to make T1 estimation with the developed pipeline more robust to noise.

2. METHODS

2.1 Bloch simulation of MOLLI sequences

As has been seen in the literature, T1 estimation through the exponential fitting of the MOLLI series assumes a monoexponential behavior in magnetization recovery affected only by T1 relaxation and, as such, has a significant systematic estimation error (51,52,57,58). Thus, if the aim is to train a Convolutional Neural Network (CNN) to accurately estimate myocardial T1 from the MOLLI series, the ground truth used to train it cannot have been obtained through exponential fitting. This presents a serious obstacle to training the CNN on experimental data obtained in a clinical setting. Instead, synthetic data has to be used.

The procedure by which synthetic MOLLI sequences have been generated is the simulation of Bloch equations. These are a set of macroscopic equations that can be used to compute the nuclear magnetization $M = [M\_x, M\_y, M\_z\ ]$ as a function of time (6,51). The meaning of the word macroscopic is that these equations do not describe the motion of individual nuclear magnetic moments. Rather, they describe the macroscopic nuclear magnetization that arises when summing up all individual nuclear magnetic moments within the sample which is what is measured in MRI.

The Bloch equations describe four distinct processes involved in the motion of the nuclear magnetization vector during MRI:

- T1 relaxation in the z-axis.
- T2 relaxation in the xy-plane.
- Nutation by a given angle about the x-axis.
- Free precession. This component is caused by the continuous rotation of the nuclear magnetization vector about the z-axis when it is excited out of equilibrium. Modern MRI processing employs a rotating frame of reference with the same angular velocity to nullify this rotation. However, differences between both angular velocities will lead to free precession.

All four processes were implemented using the framework described in (57):

- T1 and T2 relaxation over a time t can be calculated through multiplication by the matrix:

$$C(t) = \begin{bmatrix} e^{\frac{-t}{T_2}} & 0 & 0 \\ 0 & e^{\frac{-t}{T_2}} & 0 \\ 0 & 0 & e^{\frac{-t}{T_1}} \end{bmatrix}, \quad (3)$$

  and addition of the vector:

$$D(t) = \left(I - C(t)\right)\begin{bmatrix} 0 \\ 0 \\ m_0 \end{bmatrix}, \quad (4)$$

where m_0 is the z-component of the nuclear magnetization vector at rest.

- Nutation about the x-axis by a given angle α, through the application of a radiofrequency pulse, can be computed through multiplication by the matrix:

$$R(\alpha) = \begin{bmatrix} 1 & 0 & 0 \\ 0 & \cos\alpha & \sin\alpha \\ 0 & -\sin\alpha & cos\alpha \end{bmatrix}. \quad (5)$$

- Free precession during a time t can be calculated by multiplication by the rotation matrix:

$$P(t) = \begin{bmatrix} \cos(2\pi\Delta f t) & \sin(2\pi\Delta f t) & 0 \\ -\sin(2\pi\Delta f t) & \cos(2\pi\Delta f t) & 0 \\ 0 & 0 & 1 \end{bmatrix}, \quad (6)$$

where Δf is the off-resonance factor defined as the difference between precession frequency and the frequency of the rotating frame of reference employed. In the current project, the effect of off-resonant free precession has been neglected since modern acquisition methods and B0 field shimming counter it very effectively (75,76). With these components, the nuclear magnetization vector at the k+1th step of a sequence (M_{k+1}) can be calculated from the nuclear magnetization vector at the kth step (M_k) as given by:

$$M_{k+1} = AM_k + B, \quad (7)$$

where the matrix A corresponds to:

$$A = P(TE)C(TE)R(\alpha)P(TR - TE)C(TR - TE), \quad (8)$$

and the vector B to:

$$B = P(TE)C(TE)R(\alpha)D(TR - TE) + D(TE), \quad (9)$$

with TE being the echo time and TR the repetition time of the acquisition.

In between sequences, only relaxation is considered. Thus, the nuclear magnetization vector after a time Δt from a sequence applied at time t is computed as:

$$M_{t+\Delta t} = C(\Delta t)M_t + D(\Delta t), \quad (10)$$

A 5(3s)3 MOLLI series (45) is composed of two inversion recovery experiments. The inversion at a time t can be simulated through the following multiplication:

$$M_{inv} = R(180º)M_t, \quad (11)$$

The procedure to simulate a 5(3s)3 MOLLI sequence is:

- Define $M_0 = [0, 0, 1]^T$
- Invert M_0
- Iterate 5 times:
    - Calculate T1 and T2 recovery of M_i since the last sequence
    - Apply a readout sequence to the recovered M_i
- Let M_i recover for 3 heartbeats and then wait for the appropriate inversion time in the next cardiac cycle.
- Invert M_i
- Iterate 3 times:
    - Calculate T1 and T2 recovery of M_i since the last sequence
    - Apply a readout sequence to the recovered M_i

Once the simulation has been performed, the 8 NMVs are rearranged according to their inversion time. Then, only the y component of the NMV is considered. The x component is null since we have assumed no free precession and the z component cannot be measured in a real setting since it is in the direction of the main magnetic field. Thus, the y component is considered a proxy of the z component. The absolute value of the y component is what will ultimately be used as the input data both for the exponential fitting and for the various DeepBLESS algorithms. This is done to represent clinical reality more accurately since the real MRI scanners used in the study only provide the absolute value of the magnetization of the tissue scanners. For a visual representation of the different orders and values of the samples simulated with a MOLLI scheme, see Figure 6.

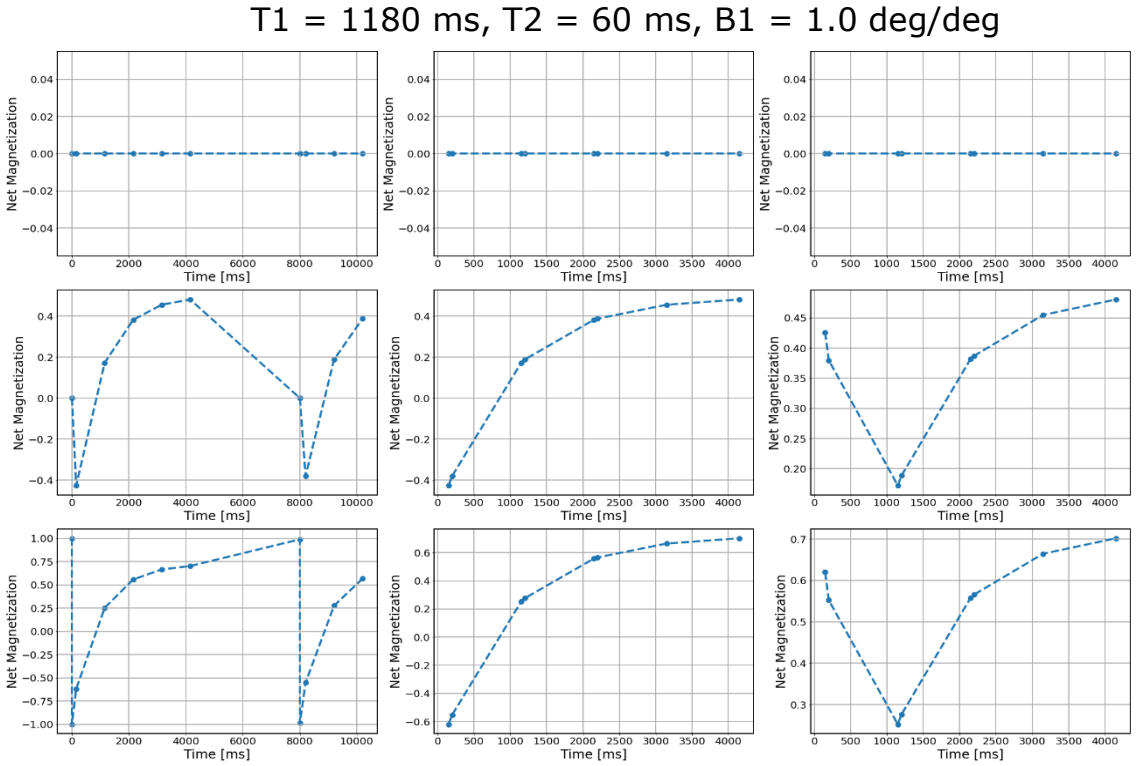

Figure 6: Three diferent visualizations of a simulated MOLLI sequence: with samples in acquisition order (left column), with samples in inversion order (middle column), and with samples in inversion order and the absolute magnetization value (right).

2.2 Dataset generation

a) From experimental TI vectors

One of the main sources of bias when estimating myocardial T1 through non-linear exponential fitting is the patient's heart rate (52). To incorporate this effect into the estimation and make it more robust to noise, the DeepBLESS-based estimation algorithms were pretrained with a set of MOLLI series simulated from real TI vectors acquired in a clinical setting. Thus, the resulting dataset, although synthetic, reflected real temporal patterns in the acquisition of the slices.

There were 27 different time vectors employed. The TI of the first acquisition in this set had a mean value of 170 ± 16 ms and a mean duration of 4497 ± 698 ms with a minimum value of 3040 ms and a maximum value of 5859 ms. The heartbeat, calculated by approximating it to the difference between the first and third inversion time, has a mean value of 59.4 ± 9.7 beats per minute with a minimum value of 33.3 bpm and a maximum value of 84.2 bpm. Such a low minimum value is possibly caused by the ECG trigger skipping a beat, which is a common cause of variability in T1 estimation, although it could also be the consequence of a bradycardic patient.

For each MOLLI series, a first 180º inversion is performed at time 0 ms, followed by a first acquisition that is simulated at a fraction 0.15 of the period of the heart. This acquisition defines the point in the heart cycle at which all of the slices will be acquired. Subsequently, a further set of 4 acquisitions were simulated, each one heart cycle apart from the other. After the fifth acquisition, the nuclear magnetization vector was let to recover for 3000 ms. Then, at a fraction of 0.2 of the period of the heart before the next acquisition point in the heart cycle, a new 180º inversion pulse was applied to the NMV. After that, three acquisitions were simulated, once again one heart beat apart from each other. For each of the 8 acquisitions, a radiofrequency pulse was simulated with a 35º degree inversion angle, which is the clinical standard for MOLLI T1 mapping sequences (73,77).

A dataset of 100,000 samples was generated through numerical simulations. This number of samples was chosen because, since we are performing a simulation within a given set of parameters, augmenting the dataset size beyond 100,000 will increase computational cost without increasing variation in the dataset significantly. The parameters T1, T2, and B1 were treated as dependent variables and randomly sampled from relevant ranges extracted from the literature (32,51) and empirically tuned to reflect those found in the experimental data (see Table 1).

	Minimum	Maximum
T1 (ms)	200	2400
T2 (ms)	20	200
B1 (deg/deg)	0.9	1.1

Table 1: Range of values from which each parameter was randomly sampled to generate a synthetic dataset.

b) From experimental T1 maps

As has been commented in the introduction, one of the main limitations of non-linear fitting for T1 estimation is the fact that it ignores spatial information. To explore how spatial information can be leveraged through DL to improve T1 estimation, a dataset of complete MOLLI series was generated using real T1 maps and time vectors. Thus, from traditionally estimated T1 maps, a synthetic MOLLI series could be generated and then used to train DeepBLESS to accurately estimate T1. The pipeline employed is illustrated in Figure 7.

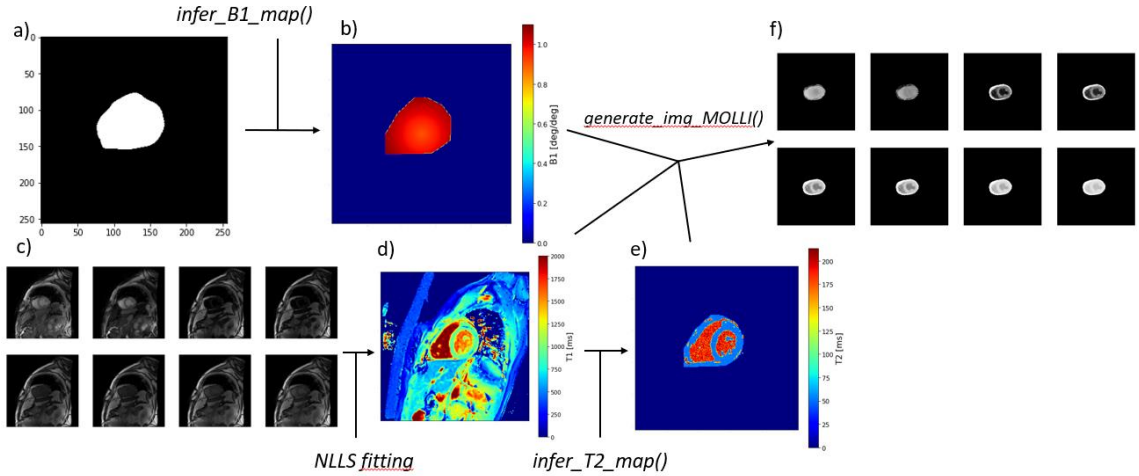

Figure 7: Diagram of the MOLLI simulation through Bloch equations from experimentally acquired MOLLI series. a) Mask of the myocardium with U-net, b) inferred B1 map, c) experimentally acquired MOLLI series, d) T1 map estimated through non-linear least-squares (NLLS) fitting, e) inferred T2 map, and f) simulated MOLLI series.

Since it was impossible to access a dataset that contained T1, T2, and B1 maps of the same patient, the same slice of the heart, and acquired simultaneously, T2 and B1 maps had to be inferred. Domain knowledge was used to do so. Thus, T2 maps were generated through the identification of tissues by their T1 value and assignment of a suitable T2 value as seen in Equation 12.

$$T_2(T_1) = \begin{cases} 52 \pm 6\ ms, & for\ T_1 < 1300\ ms \\ 186.1 \pm 27.0\ ms, & for\ T_1 \geq 1300\ ms \end{cases}, \tag{12}$$

Only two types of tissues were considered, blood and myocardium, since those are the clinically relevant ones. Thus, the inference was only performed in the region of the image corresponding to the heart. The method used for segmentation of the heart will be explained in Section 2.3b.

On the other hand, B1 maps were geometrically simulated. For an image with shape m x n, the distance from each pixel to the center of the image (the pixel (m/2, n/2)) was calculated as:

$$D = \sqrt{x^2 + y^2}, \tag{13}$$

where x and y are the horizontal and vertical distance in pixels to the center. This distance was then scaled between 0.9 deg/deg and B1_max. B1_max is calculated as,

$$B1_{max} = \frac{(1 - 0.9) \cdot \frac{m}{2} \cdot \frac{n}{2}}{radius} + 0.9\,, \qquad (14)$$

which ensures that the values within the heart mask are realistic, between 0.9 and 1.1 deg/deg, a ±10% variation in flip angle.

Once all maps were obtained or simulated, they were used along with the time vector of the experimental acquisition, to generate a synthetic MOLLI series through numerical simulation of Bloch equations. The simulation was composed of 8 images with differing degrees of contrast and intensity, from which T1 estimation could be performed. To generate the dataset from experimentally acquired data, a dataset composed of 27 single-slice MOLLI series acquired with the 5(3s)3 protocol using a b-SSFP readout at a main magnetic field strength of 3 Tesla.

2.3 Data pre-processing

a) Normalization

An optimal training of a DL algorithm requires both its inputs and its outputs to be on a similar scale of around 1. In the case of T1 estimation, normalization will be required to achieve this. Since, in this project, the magnetization is simulated, it is already normalized between 0 and 1. Thus, only the time vector and the parameters must be normalized. The normalization they underwent was the following:

- Time vector: Normalized by dividing it by 5000 ms.
- T1: Normalized by dividing it by 2400 ms.
- T2: Normalized by dividing it by 200 ms.
- B1: Minmax normalization with the range of values seen in Table 1.

Each parameter is normalized differently so that the estimation accuracy of each parameter impacts the cost function equally during training.

b) Heart segmentation

When acquiring a MOLLI series for myocardial T1 estimation, not only the heart is imaged. Numerous other tissues and organs, as well as the air surrounding the patient, are also imaged. However, when training a Deep Learning algorithm for cardiac T1 estimation, the focus is on estimating myocardial and blood T1. Thus, a way of selecting only the region of interest in the MOLLI series is needed.

Prior to constructing a dataset of single-pixel MOLLI series and its corresponding parameter, heart segmentation was performed. To do so, the same U-net model (78) as in Iglesias et al. (74) was used. Subsequently, all segmentations were refined by deleting all mask objects except the largest one. Thus, only the real heart mask was kept, and artifacts generated during the masking process were removed from the mask.

c) Adding noise for data augmentation

In a clinical setting, MOLLI acquisition cannot perfectly capture the magnetization processes that underly MRI imaging due to the interference of external factors. These interferences translate into noise that is present in the slices and degrades image quality.

To make the Deep Learning estimation of T1 robust to the noise present in the real MOLLI series, noise was added to the synthetic series generated with Bloch equations simulation. Two different kinds of noise were applied to the synthetic MOLLI series: additive thermal noise, and impulse noise. Additive thermal noise reflects the limited signal-to-noise ratio of the acquisition and was simulated by adding to each sample a random value between 0 and 0.01. Impulse noise reflects the effect of artifacts such as patient movement which may appear while scanning, and it was simulated by multiplying a sample by a random float number between 0.9 and 1.1 with a 5% probability. A simulated MOLLI can be seen in Figure 8 before and after having noise added to it.

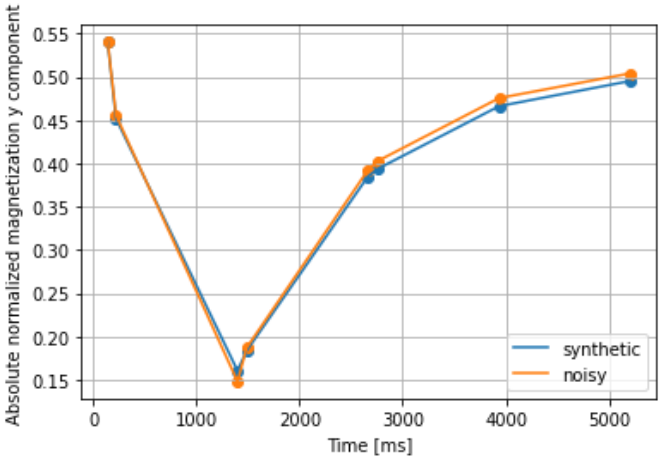

Figure 8: Plot of a simulated pixel of a MOLLI series before and after noising.

d) Median and neighbors dataset assembly

The datasets to train the median and neighbors' variants of the DeepBLESS architecture required an additional step to assemble. In the case of the median dataset, first, the MOLLI series were processed with a median filter. Then each pixel's intensity and the median obtained in the previous step are stored in a 3 by 8 array, as part of an N by 3 by 8 array where N is the number of samples. For the neighbors' dataset, each neighbor of the pixel must belong to the heart mask for that pixel to be included in the dataset. Each neighboring pixel is stored in a row from the 2nd to the 9th in a 10 by 8 array, where the first and last row are occupied by the pixel of interest and the sampling vector respectively. All samples are stored in a larger array similar to the one described for the median dataset.

2.4 T1 estimation

a) Exponential fitting

The conventional way of estimating myocardial T1 is through the exponential fitting of the 8 temporal samples acquired for each pixel. Such a process is usually performed

through Levenberg-Marquardt or non-linear least-squares fitting (79). The three-parameter function,

$$y = A - Be^{-\frac{t}{T_1^*}}, \tag{14}$$

is iteratively fitted until an optimal solution is reached from which T1 is estimated as,

$$T1 = T1^* \cdot \left(\frac{B}{A} - 1\right), \tag{15}$$

However, since the MOLLI series employed in the current project record the absolute value of the magnetization, exponential fitting cannot be performed directly on the 8-pixel values. Thus, the algorithm used to estimate T1 is applied several times to the data, with progressively more samples multiplied by -1. Then, the fit with the smallest estimation error is chosen as the correct one, and its estimation is recorded as the T1 value of the specific pixel.

b) DeepBLESS

STANDARD DEEPBLESS

DeepBLESS is a deep convolutional neural network consisting of a sequence of 3 convolutional layers with 4 ResNet blocks between the first and second convolutional layer and a dense layer as the output layer (see Figure 4). All convolutional layers have 32 filters with a 3x1 size and a stride of 1 except for the last 2 which use a stride of 2. The input layer has a size of 2x8 which consists of a 1-D temporal signal. The first row or channel corresponds to the 8 intensities of a single pixel in the MOLLI series and the second channel corresponds to the 8 TIs at which slices are acquired. The dense layer has an output of size 3 to estimate each of the 3 parameters: T1, T2, and B1. The activation function of every layer is the Rectified Linear Unit function (80). The total number of trainable parameters is 32,099.

The network was pretrained on a set of 100,000 synthetic MOLLI sequences generated from experimental TI vectors for 3000 epochs. Finally, it was trained for 3000 epochs on a set of 151,117 synthetic MOLLI series generated from experimental TI vectors and T1 maps with added noise, combined with another 100,000 samples generated from experimental TI vectors with the parameter ranges presented in Table 1 . A validation set with a size of 10% of the training set was defined and used to evaluate performance during training and the final performance of the model. The used cost function was the mean squared error (81) and the optimizer chosen, Adam (82)

MEDIAN-DEEPBLESS

Median-DeepBLESS is a convolutional neural network that differentiates itself from DeepBLESS in its input layer. Its size is 3x8 and it incorporates a second 1-D signal that encodes the median value of the neighborhood of the pixel in each of the 8 acquisitions. The total number of trainable parameters of this model is 32,099.

Median-DeepBLESS was first pretrained with a synthetic dataset of 100,000 samples for 3000 epochs. That dataset was generated in the way described in the chapter Section 2.2a

with the addition that each individual pixel's intensities were repeated in the second row of the input samples. The final training was performed on a dataset of 151,117 samples simulated from experimentally acquired data in the way described in Section 2.2b combined with another 100,000 samples generated from experimental TI vectors with the parameter ranges presented in Table 1 for 3000 epochs. For both training stages, a validation set of 10% was split from the training set to ensure correct training. The validation set from the second training was employed to evaluate the performance of the algorithm on unseen data. The cost function and optimizer were the same as for DeepBLESS.

NEIGHBORS-DEEPBLESS

Neighbors-DeepBLESS is a convolutional neural network that also differentiates itself from DeepBLESS in its input layer. Its size is 10x8 as it incorporates 8 1-D signals in addition to the intensities of the pixel of interest. Those signals encode the intensity values of each of the 8 neighboring pixels in each of the 8 acquisitions.

Neighbors-DeepBLESS was first pretrained with a synthetic dataset of 100,000 samples generated in the way described in Section 2.2a with the addition that each individual pixel's intensities were repeated in the second to ninth rows of the input samples. The final training was performed on a dataset of 141,782 samples simulated from experimentally acquired data in the way described in Section 2.2b combined with another 100,000 samples generated from experimental TI vectors with the parameter ranges presented in Table 1 for 3000 epochs. For both training stages, a validation set of 10% was split from the training set to ensure correct training. The validation set from the second training was employed to evaluate the performance of the algorithm on unseen data. The cost function and optimizer were the same as for DeepBLESS.

3. RESULTS

3.1 Characterization of generated datasets

a) From experimental TI vectors

To pretrain each DeepBLESS-like model, a synthetic dataset of the MOLLI series was simulated from real sampling patterns of the MOLLI series. Such dataset was composed of 100,000 samples with a uniform parameter distribution, as seen in Figure 9.

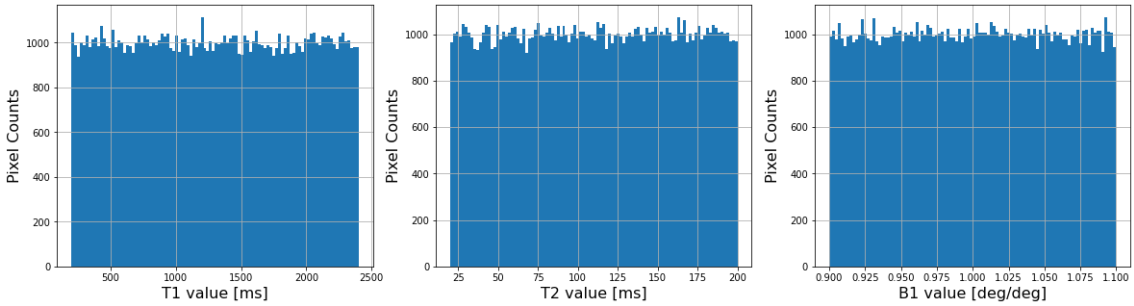

Figure 9: Histogram of parameter values for the dataset simulated from experimental MOLLI sampling time vectors.

b) From experimental maps

To train the DeepBLESS-like models, a synthetic dataset of MOLLI series was simulated from real sampling patterns of MOLLI series, and the T1 maps estimated in clinical routine from a given experimentally acquired MOLLI series. This dataset was fused with a synthetic dataset of MOLLI series simulated only from real TI vectors and with a wider range of parameters to increase diversity in the training set.

This dataset was composed of 151,117 samples with the parameter distribution seen in Figure 10. The values of T1 exhibit two peaks that roughly coincide with T1 values of the myocardium and the blood. The large peak at 2000 ms corresponds to the maximum value of T1 present in the real T1 maps, which probably condenses all values above it to 2000 ms.

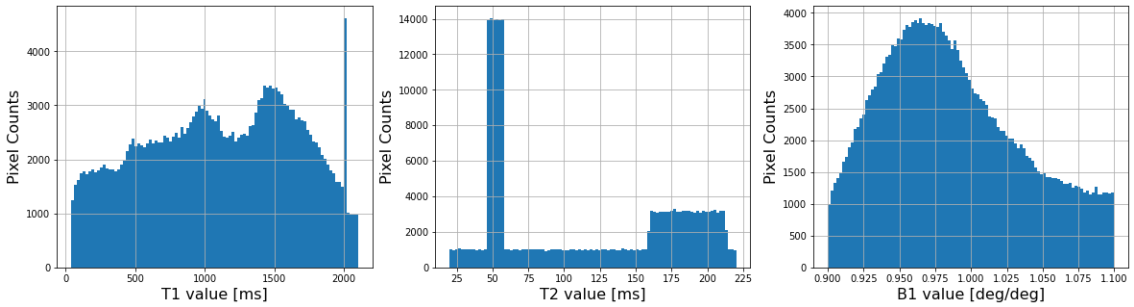

Figure 10: Histogram of parameter values for the dataset simulated from experimentally acquired T1 maps

3.2 Training and validation loss

In Figure 11 the training and validation loss of the 3 DeepBLESS-based architectures can be seen. The three training processes show correct learning although a widening difference between training and validation loss can be seen by the end of the training protocol. Both validation and training loss were the lowest and highest for median-DeepBLESS and neighbors-DeepBLESS, respectively.

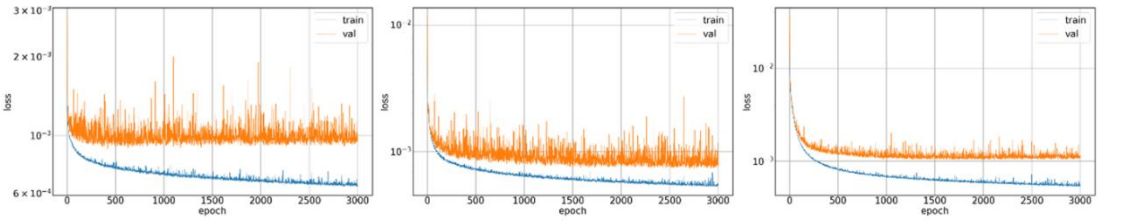

Figure 11: Training and validation loss of a) DeepBLESS, b) median DeepBLESS and c) neighbors DeepBLESS.

The performance metrics evaluated on the validation set for each algorithm can be found in Table 2. As can be seen, both the mean absolute error and the mean relative error in the case of the exponential fitting are much larger than in either of the DeepBLESS-based estimators. The best performing approach as measured by these metrics is Median-DeepBLESS whilst Neighbors-DeepBLESS seems to be the worst performing of the DL approaches.

	T1		**T2**		**B1**	
	MAE [ms]	MRE [%]	MAE [ms]	MRE [%]	MAE [deg/deg]	MRE [%]
Exponential fitting	138 ± 90	9.01 ± 4.9	-	-	-	-
DeepBLESS	14 ± 9	3.37 ± 3.04	9 ± 7	8.01 ± 5.49	0.004 ± 0.003	0.446 ± 0.312
Median-DeepBLESS	13 ± 9	3.09 ± 2.75	7 ± 5	6.38 ± 3.8	0.003 ± 0.002	0.327 ± 0.229
Neighbors-DeepBLESS	23 ± 17	6.48 ± 6.16	10 ± 8	10.24 ± 8.15	0.003 ± 0.003	0.345 ± 0.254

Table 2: Mean absolute error and mean relative error for each parameter (T1, T2, and B1) with each estimation algorithm.

3.3 Estimation accuracy

To quickly visualize the general accuracy of T1, T2, and B1 estimation by the different algorithms, a scatter plot of the estimation value with respect to the real value was drawn (see Figure 12). The closer the points are to the identity (red) line, the better the estimation is. This scatter plot allows visualizing whether the estimations roughly coincide with the real parameters.

In the case of T1 estimation by means of exponential fitting, a clear bias can be established. Exponential fitting tends to underestimate T1, and such underestimation increases with T1. Standard DeepBLESS and median-DeepBLESS both estimate most values on top of the red line. However, median-DeepBLESS seems to have a few outliers that are further from the true estimation than in the case of standard DeepBLESS. Finally,

when it comes to neighbors-DeepBLESS, estimations are also clustered around the identity line, although a larger variance is observed in some outliers.

When looking at T2 estimation it must be taken into account the fact that the values of T2 present in the dataset are only those corresponding to blood and myocardium. That is why both estimation and real T2 values form two clusters around 50 and 180 ms respectively.

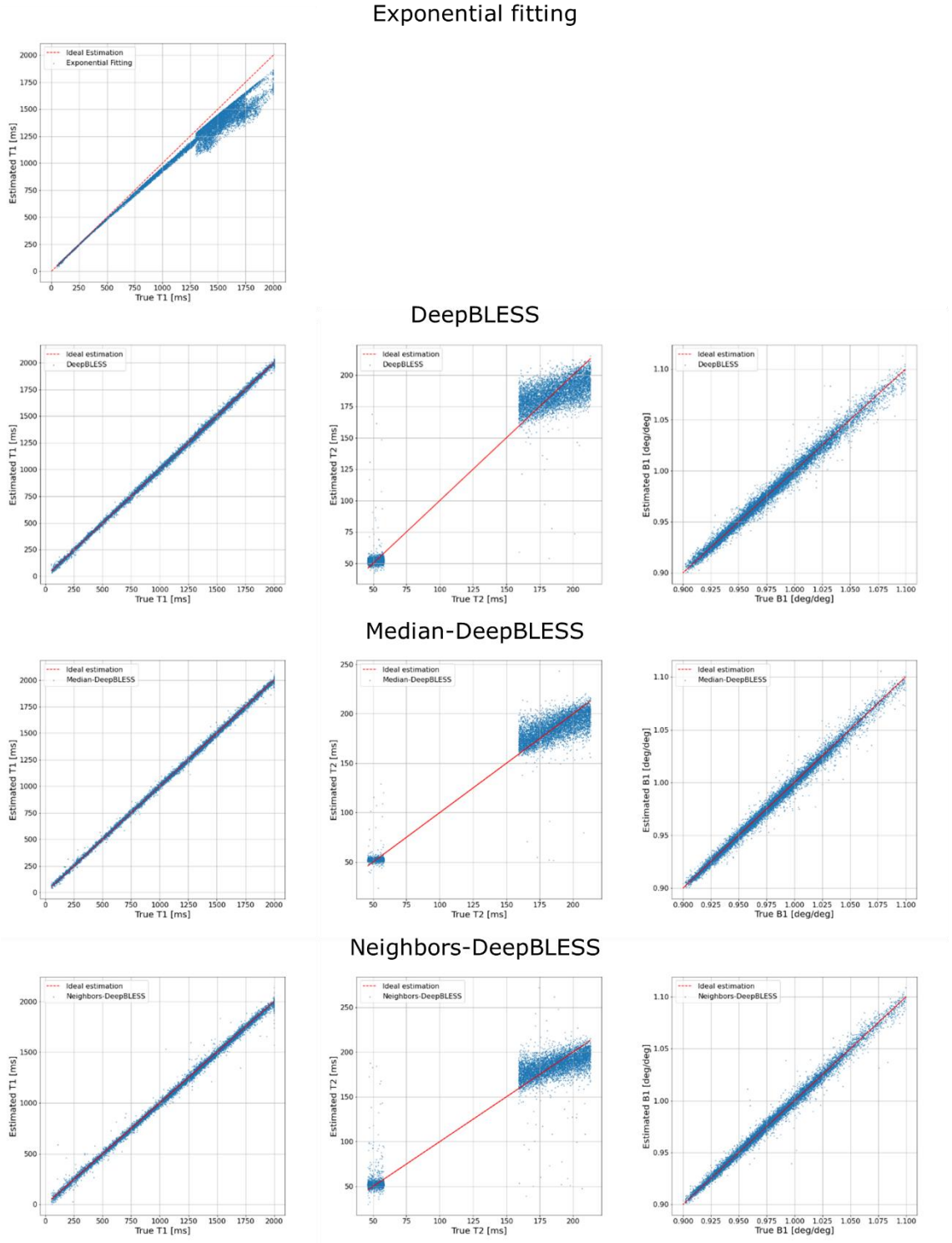

Figure 12: Scatter plots relating the estimation of each parameter (T1, T2, and B1), to its true values for each estimation algorithm.

Nevertheless, it can be seen that there is some correlation between estimated and true T1 within those clusters. However, estimation errors are much more noticeable than in the case of T1. All three DeepBLESS variants performed very similarly in this task.

Finally, with respect to B1 estimation it can be seen that similarly to T1 estimation, it is clustered around the identity line, although with larger dispersion. The estimation deviation seems to be smaller for Median-DeepBLESS than for the other two algorithms, although any differences are slight.

To further characterize the estimation errors committed by each approach, Bland-Altman plots were computed. These are a type of plot that is very useful to analyze whether there are any trends in the error and so, whether there is a certain bias in the estimation. The focus will be on the effect of the parameter values on the estimation of T1 since that is the main aim of the current project. Nevertheless, a similar analysis has been performed for T2 and B1 estimation through DeepBLESS and its spatially-aware variants, and it can be found in SI-1.

In Figure 13 the Bland-Altman plots of the T1 estimation error with respect to the T1, T2, and B1 values of the sequence are displayed. In the case of exponential fitting, it can be seen that the mean T1 estimation error is -104 ± 90 ms which corresponds to a significant underestimation of T1 values. Such underestimation is directly correlated with increasing T1. In relation to T2, it can be seen that for larger T2 values (those in the blood cluster), T1 underestimation increases. With regards to B1, a clear pattern of larger underestimation is observed towards the lower end of the spectrum (0.9 deg/deg). There appear to be two distinct horizontal clusters of points, stretching out diagonally towards the lower-left corner of the plot.

In the case of the DeepBLESS variants, we can see that the systematic bias in T1 estimation is greatly reduced in comparison to exponential fitting. DeepBLESS and Median-DeepBLESS both display a mean estimation error of 2 ± 14 ms whilst Neighbors-DeepBLESS presents a mean estimation error of -4 ± 22 ms. Thus, the underestimation bias present in exponential fitting has either been completely eliminated (DeepBLESS and Median-DeepBLESS) or reduced by a factor of 26 (Neighbors-DeepBLESS), and the random estimation errors as measured by the standard deviation have been reduced by a factor of 6.5 and 4.1 respectively. Furthermore, the relationship between larger T1 values and T1 underestimation seems to have disappeared.

With regards to the effect of T2 on T1 estimation through DeepBLESS and its variants, a bi-cluster shape can be observed with two distinct clouds of points around the values of blood and myocardial T1 respectively. Unlike in the case of exponential fitting, there seems to be no correlation between T2 values and estimation errors in T1.

Finally, with respect to B1, it seems to have no noticeable impact on T1 estimation error with the DeepBLESS-based approaches. The only discernible trend is a smaller number of outliers near the larger end of the B1 spectrum, although at that end of the scale there is also a smaller number of samples compared to other sections of the B1 range.

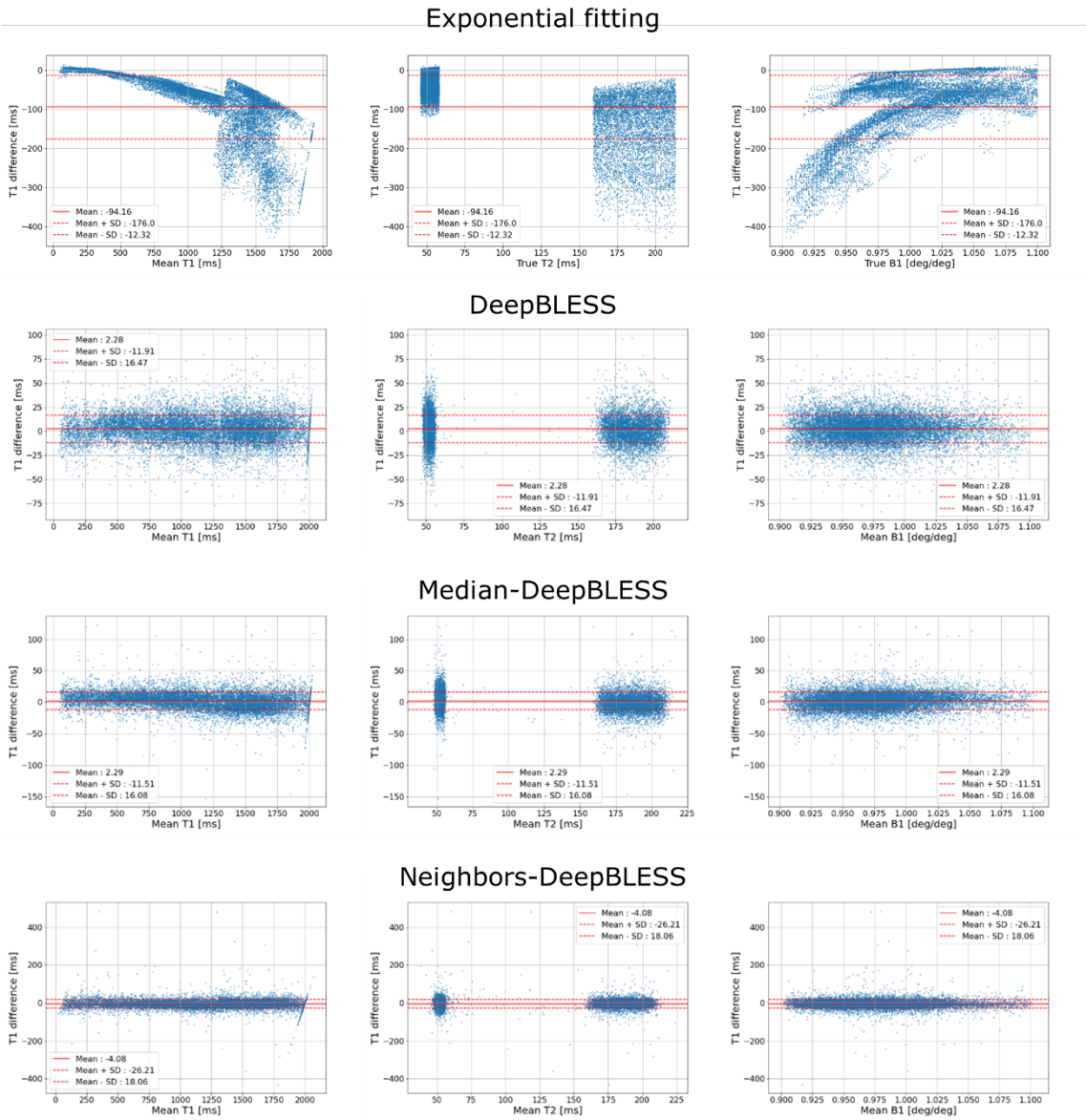

Figure 13: Bland Altman plots of the T1 estimation error with relation to the mean value of each parameter (T1, T2, and B1).

3.4 Whole map estimation

A sample T1 map is displayed in Figure 14, which has been estimated with each of the four approaches employed in the current thesis. Pixels corresponding to blood are colored red due to their high T1 values, while pixels corresponding to myocardium take a yellow, green, or blue color. It can be easily appreciated that the map estimated through exponential fitting presents a lighter color scheme than the rest of the maps which aligns with the underestimation tendency presented in Section 3.3.

Figure 14 also includes a visual representation of the difference between each estimated map and the reference map (one estimated in clinical practice from real MOLLI sequences and used to simulate the MOLLI sequence employed as input for the estimation), where red indicates overestimation and blue indicates underestimation. In these visualizations, the underestimation of T1 by exponential fitting can be clearly seen. It is apparent that the largest estimation error appears in the pixels depicting blood. When it comes to the

DeepBLESS-based networks, the estimation errors are much smaller, as shown by the lighter shades of red and blue displayed. There seems to be a tendency in all three algorithms to overestimate the T1 values of the blood and underestimate those of the myocardium. Median-DeepBLESS seems to be the best performing of the three since it presents numerous patches of white over the heart, indicating very small or inexistent estimation errors. On the other hand, Neighbors-DeepBLESS seems to be the worst performing of the three.

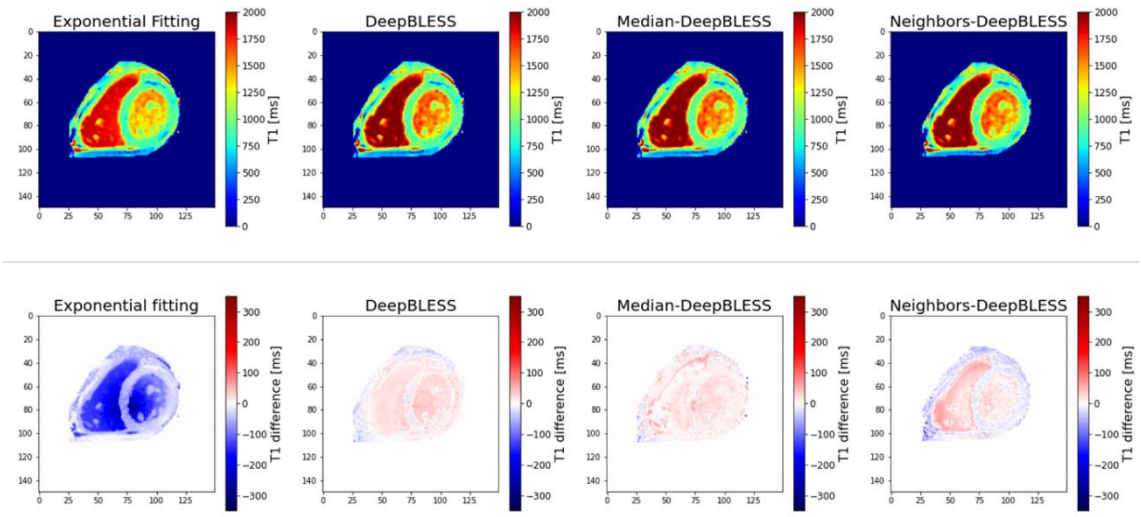

Figure 14: Reconstructed T1 maps estimated with each different algorithm (first row) and colored visualizations of the difference between the estimated maps and the reference map (second row).

In Figure 15, the estimated T2 maps employing the three DL approaches can be observed. A clear distinction is seen between the myocardium (blue) and the blood pool (red), although some patches of red are interspersed within the blue and vice versa.

In each of the three algorithms, the estimation error on the pixels depicting blood seems to be much higher than on the pixels depicting myocardium. Additionally, it seems that the algorithms tend to overestimate the T2 values in the myocardium and underestimate those in the blood. This effect is strongest in DeepBLESS, and it is lower in Median-DeepBLESS and Neighbors-DeepBLESS.

The estimated maps corresponding to B1 inhomogeneities are presented in Figure 16, along with the colored visualizations of the estimation error. It can be seen that all three algorithms have correctly reproduced the radial pattern of the inferred T1 map. However, it can also be appreciated that the anatomy of the heart seems to influence the estimation, with a seemingly noisier estimation in the regions corresponding to the myocardium. The color-coded difference map shows that all three algorithms generally underestimate B1 for these MOLLI series. The before-mentioned influence of the heart's anatomy on B1 estimation can also be appreciated in the difference maps, with a much noisier B1 estimation in areas corresponding to the myocardium.

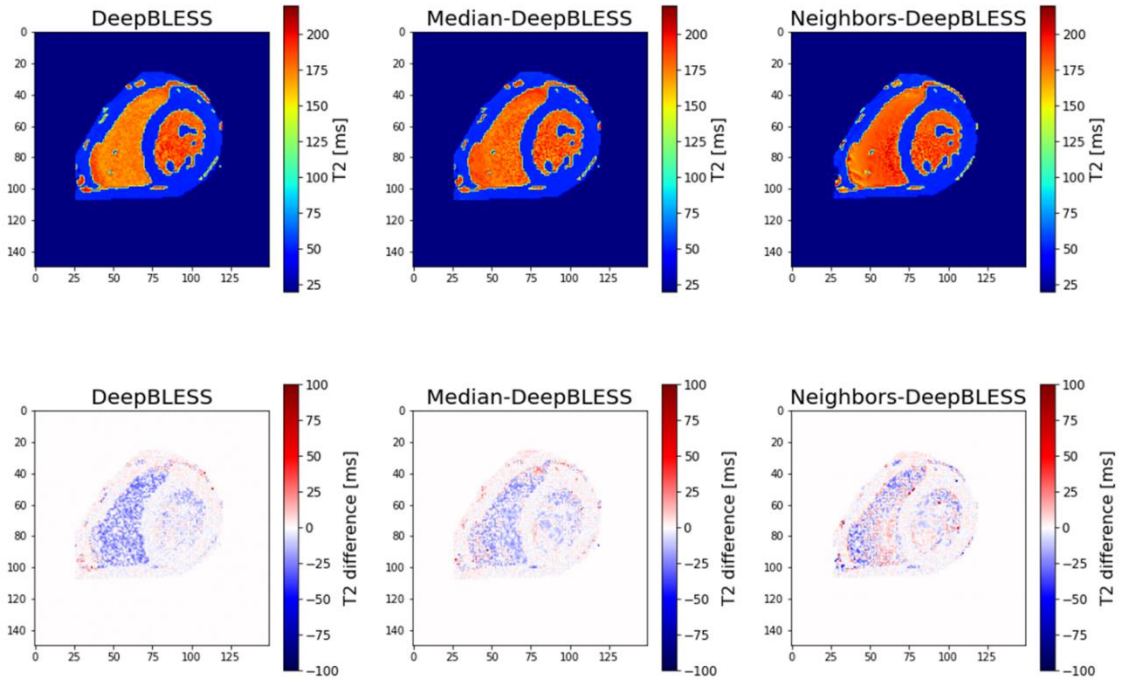

Figure 15: Reconstructed T2 maps estimated with each different algorithm (first row) and colored visualization of the difference between the estimated maps and the reference map (second row).

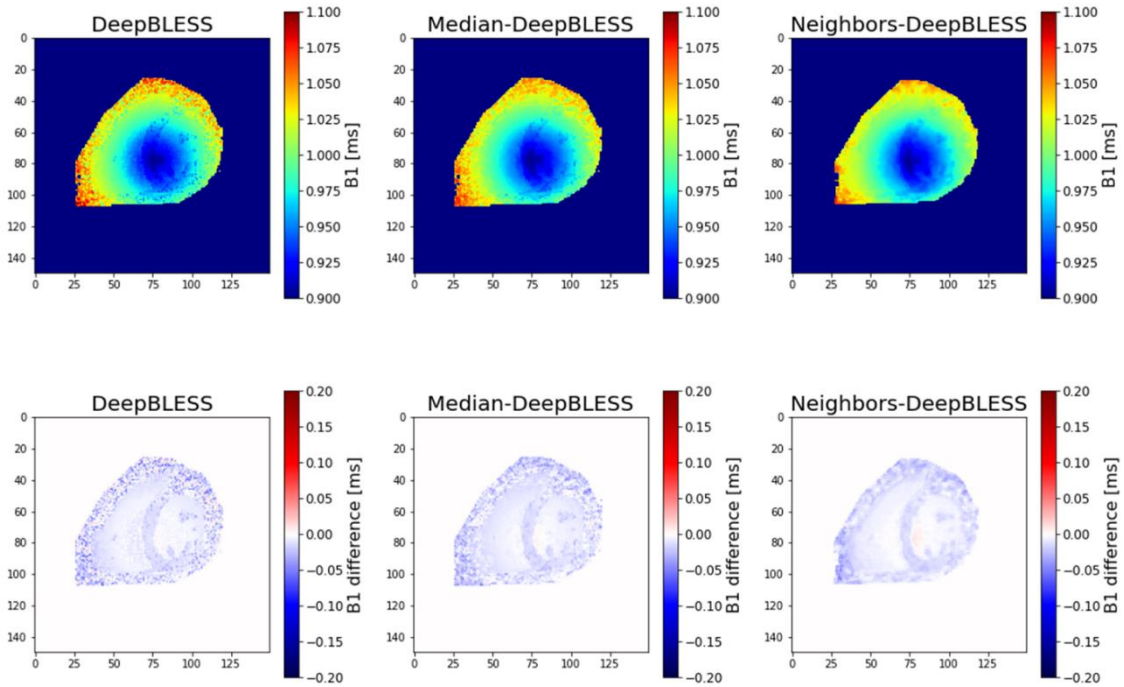

Figure 16: Reconstructed B1 maps estimated with each different algorithm (first row) and colored visualization of the difference between the estimated maps and the reference map (second row).

3.5 Robustness to noise

In Figure 17, the estimated T1 maps from a simulated MOLLI sequence that has been noised with the procedure described in Section 2.3c can be seen. In a similar manner to the maps displayed in Figure 14, a clear underestimation bias can be observed in the case of exponential fitting, which overshadows any effects of the noise. In the case of the three

DL estimators, once again it can be seen that Median-DeepBLESS is the best performing of the three since it displays swaths of white pixels and a less marked relationship between over/underestimation and different tissues (blood and myocardium). DeepBLESS and Neighbors-DeepBLESS on the other hand, display larger estimation errors. The former has a tendency to overestimate blood T1 whilst the latter has a strong tendency to underestimate myocardial T1.

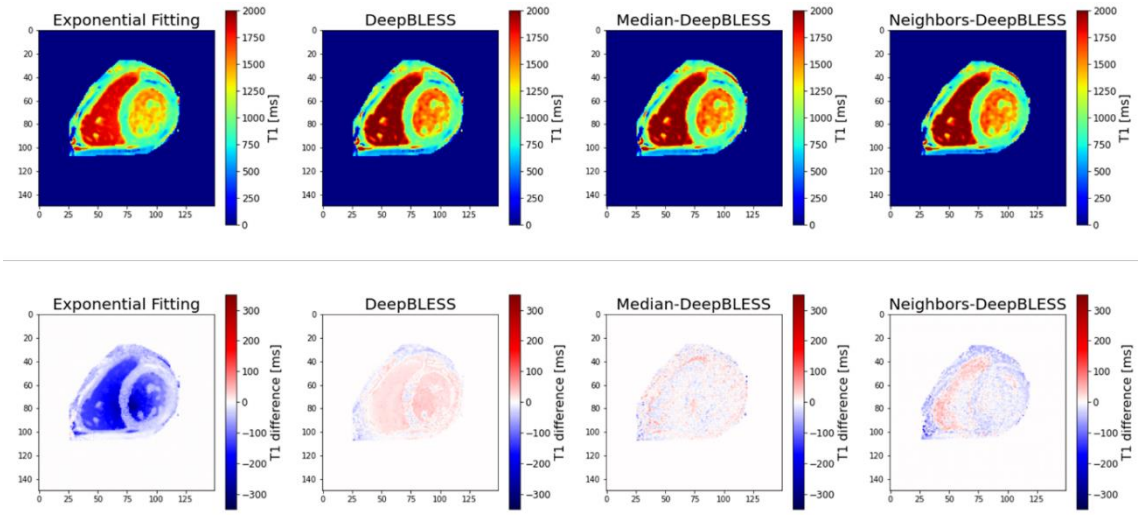

Figure 17: Reconstructed T1 maps estimated from noisy simulated MOLLI sequences with each different algorithm (first row) and colored visualization of the difference between the estimated maps and the reference map (second row).

4. DISCUSSION

It has been documented in the literature that MOLLI acquisition and T1 estimation from MOLLI series through standard exponential fitting leads to significant underestimation of T1 due to the combination of modulated and unmodulated magnetization recovery within the acquisition scheme (51,52). Additionally, it has also been reported that variations in T2 and flip angle (caused by inhomogeneities in B1), also impact T1 estimation accuracy (57). Thus, the T1 estimation errors reported in Section 3.3 when performing pixel-wise exponential fitting of MOLLI sequences are largely in agreement with the available literature.

On the other hand, the proposed DL approaches for T1 estimation have shown the capability of correcting those biases in T1 estimation, in comparison with previous studies using DL (74). The underestimation tendency has been erased and the influence of T2 and B1 variations have been counteracted, as can be seen in Figure 12 and Figure 13. Furthermore, the precision of T1 estimation has also improved when using DeepBLESS-based methods, as the standard deviation of T1 estimation error has been reduced significantly when compared with exponential fitting.

A further advantage of DL approaches as opposed to exponential fitting is their ability to approximately estimate the values of T2 and B1 from an acquisition sequence that was mainly and chiefly designed to capture T1 relaxation in the tissue. Nevertheless, it has been shown, as can be seen in Figure 13, that the DeepBLESS architecture is capable of identifying the effects of these interfering factors in MOLLI. This is quite relevant since it opens the door to the simultaneous acquisition of T1 and T2 using a single sequence that is already well established in clinical practice. Additionally, it also offers the chance of assessing inhomogeneities in B1 that may have been present during the acquisition of the sequence, something which is seldom done in routine clinical practice.

With respect to DeepBLESS' potential to incorporate spatial information for improving T1 estimation and making it spatially-aware, it has been shown that Median-DeepBLESS outperforms standard DeepBLESS both in the presence and absence of noise, similar to the results of Iglesias et al. (74). It seems that Median-DeepBLESS is the optimal strategy to incorporate spatial information into the T1 estimation process by means of Deep Learning. On the contrary, the strategy used in Neighbors-DeepBLESS seems to be counterproductive, since its performance is worse than that of standard DeepBLESS. That might be due to the fact that it minimizes the information contribution of the pixel of interest in the input sample, and it incorporates too much information that may be contradictory in the case of pixels next to an edge in the image.

Nevertheless, the performance of the best-performing models should be further validated, since they have only been trained and evaluated on simulations of MOLLI sequences, albeit from experimental data. This is especially problematic in the case of T2 and B1 prediction since they have been inferred using domain knowledge and they may not totally represent the clinical reality of patients' physiology. Furthermore, the dataset used has been small (N = 28) and from a single scanner. It is known that CNNs can be highly sensitive to scanner vendor, although since the models proposed only consider single pixels or 3x3 kernels of pixels, they may be less susceptible to such an effect.

Even though results in the current project are encouraging, further research is needed to definitively validate the models and implement them into clinical practice. The main area in which there is room for improvement is the dataset used to train the algorithms. As has been commented before, the T2 and B1 maps used to train the algorithm have been generated using domain knowledge as described in Section 2.2b. This means that although they might approximately represent clinical reality, they are not realistic enough for a thorough validation of DeepBLESS estimation performance. One way of addressing this issue would be to simulate MOLLI sequences using clinically acquired maps of T2 and B1 in addition to T1. A technique that might allow that is low-rank reconstruction, which is a method for simultaneous multislice acquisition of T1 and T2. Data acquired through this technique would eliminate the need for registration of T1 and T2 maps from a single patient. In conjunction with B1 maps acquired through the Bloch-Siegert method (83), this data could be used to simulate MOLLI sequences pixel by pixel with parameter values that represent real myocardial tissue in health and disease.

To validate the DeepBLESS-based approaches on real MOLLI data and not just simulations, a hybrid dataset consisting of MOLLI and SR sequences could be employed. Thus, the models could be trained on the MOLLI sequences to predict the SR estimation values. Nevertheless, this method may encounter problems with the misregistration of the two different acquisitions and lack of reproducibility of T1 values with each technique. Furthermore, it would lack the data needed to validate the estimation of T2 and B1 from MOLLI, which is one of the main advantages of using DL over exponential fitting methods.

In order to overcome the dataset size and diversity issue, DeepBLESS models should be trained on a larger database of MOLLI sequences. This dataset should be sourced from multiple centers and vendors to ensure its generalization to unseen data and make it robust to centers' slight differences in procedure.

Finally, it would be interesting to test new architectures that might improve estimation performance or maybe even overcome the issue with ground truth generation altogether. Approaches have been proposed to employ adversarial architectures as a way of generating specific MRI images from other acquisitions (84). There have also been proposals for using parallel estimation pipelines to identify and correct the effect of confounders such as free precession and heart rate variability on the estimation of T1 (Rui et al., ISMRM, 2022).

5. CONCLUSION

Despite its shortcomings when capturing and estimating T1 in myocardial tissue, the MOLLI acquisition sequence continues to be the standard for myocardial T1 estimation in clinical routine. This is mainly due to its reproducibility (11), the fact that it has been clinically validated for a large number of myocardial pathologies (3,12,15,20–30), along with the bias of clinical stakeholders toward already established procedures and protocols. In the current project, it has been established that DL approaches to myocardial T1 estimation can in principle solve the issues associated with the use of MOLLI to acquire magnetization recovery data.

Firstly, it has been shown that simulation of Bloch equations offers a way of generating a dataset from clinical data that overcomes the bias in the ground truth obtained by conventional estimation methods. This is shown by the fact that exponential fitting of simulated data consistently underestimates T1, in agreement with published literature (52). Additionally, its potential for considering the presence of confounders such as T2 and B1 has also been explored.

Related to this first finding is the fact that DeepBLESS-based networks trained on Bloch simulations do not display any underestimation bias of T1, unlike is the case for exponential fitting. They are also able to counter the effect of parameters that interfere with magnetization recovery as captured in MOLLI sequences, namely T1 and T2. Furthermore, they have been shown capable of estimating those confounders with relative accuracy, which opens the door to simultaneous quantification of several parameters from a well-established clinical acquisition scheme as is MOLLI.

Finally, Median-DeepBLESS, a spatially-aware variant of the DeepBLESS architecture, has been shown to improve estimation accuracy and resilience to noise, beyond what is possible with both exponential fitting and the standard DeepBLESS network. This is significant since it may allow accurate T1 mapping with worse image quality which often comes as a result of faster scan times. Thus, spatially-aware DL approaches have the potential to improve patient throughput in a clinical setting.

All in all, the current project presents a proof of concept for a DL approach that corrects the inherent biases in the estimation of T1 from MOLLI, whilst providing approximate quantification of confounders and improved robustness to degraded image quality. In the future, this may allow for improved quantification of tissue parameters in the heart using an already well-established acquisition sequence.

BIBLIOGRAPHY

1. Damadian R, Goldsmith M, Minkoff L. NMR in cancer: XVI. Fonar image of the live human body. Physiological Chemistry and Physics. 1977;9(1):97–100.
2. Benefits and Risks | FDA [Internet]. [cited 2022 Jun 12]. Available from: https://www.fda.gov/radiation-emitting-products/mri-magnetic-resonance-imaging/benefits-and-risks
3. Rajiah P, Desai Y, Kwon D, Flamm SD. MR Imaging of Myocardial Infarction. RadioGraphics [Internet]. 2013;33(5):1383–413. Available from: http://radiographics.rsna.org/lookup/suppl/doi:10.1148/rg.335125722/-/DC1.
4. Ge Y. Multiple Sclerosis: The Role of MR Imaging. American Journal of Neuroradiology [Internet]. 2006 Jun;27:1165–76. Available from: www.ajnr.org
5. Bushong S, Clarke G. Magnetic Resonance Imaging: Physical and Biological Principles [Internet]. 4th ed. Elsevier. Elsevier; 2015 [cited 2022 Jun 12]. 492 p. Available from: https://books.google.co.id/books?hl=id&lr=&id=Xe9OAQAAQBAJ&oi=fnd&pg=PP1&dq=Magnetic+Resonance+Imaging:+Physical+and+Biological+Principles+4th+Edition&ots=jonELt0y5E&sig=__JVaF2MaMYLXFNPqj7fSlgG8hE&redir_esc=y#v=onepage&q=Magnetic Resonance Imaging%3A Phy
6. Bloch F. Nuclear Induction. Physical Review. 1946 Oct;70(7–8):460–73.
7. Bloembergen N, Purcell EM, Pound RV. Relaxation Effects in Nuclear Magnetic Resonance Absorption. Physical Review. 1948 Apr 1;73(7):679–712.
8. Allisy-Roberts PJ, Williams J. Farr's Physics for Medical Imaging: Second Edition. Farr's Physics for Medical Imaging: Second Edition. Elsevier Inc.; 2007. 1–207 p.
9. Bottomley PA, Foster TH, Argersinger RE, Pfeifer LM. A review of normal tissue hydrogen NMR relaxation times and relaxation mechanisms from 1-100 MHz: Dependence on tissue type, NMR frequency, temperature, species, excision, and age. Medical Physics. 1984 Jul;11(4):425–46.
10. Moon JC, Messroghli DR, Kellman P, Piechnik SK, Robson MD, Ugander M, et al. Myocardial T1 mapping and extracellular volume quantification: A Society for Cardiovascular Magnetic Resonance (SCMR) and CMR Working Group of the European Society of Cardiology consensus statement. Journal of Cardiovascular Magnetic Resonance. 2013;15(1).
11. Taylor AJ, Salerno M, Dharmakumar R, Jerosch-Herold M. T1 Mapping Basic Techniques and Clinical Applications. Vol. 9, JACC: Cardiovascular Imaging. Elsevier Inc.; 2016. p. 67–81.
12. Messroghli DR, Niendorf T, Schulz-Menger J, Dietz R, Friedrich MG. T1 Mapping in Patients with Acute Myocardial Infarction. Journal of Cardiovascular Magnetic Resonance. 2003;5(2):353–9.
13. Messroghli DR, Radjenovic A, Kozerke S, Higgins DM, Sivananthan MU, Ridgway JP. Modified look-locker inversion recovery (MOLLI) for high-resolution T1 mapping of the heart. Magnetic Resonance in Medicine. 2004;52(1):141–6.
14. Jerosch-Herold M, Sheridan DC, Kushner JD, Nauman D, Burgess D, Dutton D, et al. Cardiac magnetic resonance imaging of myocardial contrast uptake and blood flow in patients affected with idiopathic or familial dilated cardiomyopathy. American Journal of Physiology - Heart and Circulatory Physiology. 2008 Sep;295(3).

15. Arheden H, Saeed M, Higgins CB, Gao DW, Bremerich J, Wyttenbach R, et al. Measurement of the Distribution Volume of Gadopentetate Dimeglumine at Echo-planar MR Imaging to Quantify Myocardial Infarction: Comparison with 99m Tc-DTPA Autoradiography in Rats 1. Radiology. 1999;211(3):698–708.
16. Poole-wilson PA, Cameron IR. Intracellular pH and K+ of cardiac and skeletal muscle in acidosis and alkalosis. AMERICAN JOURNAL OF PHYSIOLOGY. 1975 Nov;229(5):1305–10.
17. Brading AF, Jones AW. Distribution and Kinetics of CoEDTA in smooth muscle, and its use as an Extracellular Marker. Journal of Physiology. 1969;387–401.
18. Ferreira VM, Piechnik SK, Robson MD, Neubauer S, Karamitsos TD. Myocardial tissue characterization by magnetic resonance imaging: Novel applications of T1 and T2 mapping. Journal of Thoracic Imaging [Internet]. 2014 [cited 2022 May 29];29(3):147–54. Available from: https://journals.lww.com/thoracicimaging/Fulltext/2014/05000/Myocardial_Tissue_Characterization_by_Magnetic.4.aspx
19. Messroghli DR, Moon JC, Ferreira VM, Grosse-Wortmann L, He T, Kellman P, et al. Clinical recommendations for cardiovascular magnetic resonance mapping of T1, T2, T2 and extracellular volume: A consensus statement by the Society for Cardiovascular Magnetic Resonance (SCMR) endorsed by the European Association for Cardiovascular Imaging (EACVI). Vol. 19, Journal of Cardiovascular Magnetic Resonance. 2017.
20. Bohnen S, Radunski UK, Lund GK, Tahir E, Avanesov M, Stehning C, et al. T1 mapping cardiovascular magnetic resonance imaging to detect myocarditis—Impact of slice orientation on the diagnostic performance. European Journal of Radiology. 2017;86.
21. Puntmann VO, Isted A, Hinojar R, Foote L, Carr-White G, Nagel E. T1 and T2 mapping in recognition of early cardiac involvement in systemic sarcoidosis. Radiology. 2017 Oct 1;285(1):63–72.
22. Aikawa Y, Noguchi T, Morita Y, Tateishi E, Kono A, Miura H, et al. Clinical impact of native T1 mapping for detecting myocardial impairment in takotsubo cardiomyopathy. European Heart Journal Cardiovascular Imaging. 2019 Oct 1;20(10):1147–55.
23. Imran M, Wang L, McCrohon J, Yu C, Holloway C, Otton J, et al. Native T1 Mapping in the Diagnosis of Cardiac Allograft Rejection: A Prospective Histologically Validated Study. JACC: Cardiovascular Imaging. 2019 Aug 1;12(8P2):1618–28.
24. Everett RJ, Stirrat CG, Semple SIR, Newby DE, Dweck MR, Mirsadraee S. Assessment of myocardial fibrosis with T1 mapping MRI. Vol. 71, Clinical Radiology. 2016.
25. Karamitsos TD, Piechnik SK, Banypersad SM, Fontana M, Ntusi NB, Ferreira VM, et al. Noncontrast T1 mapping for the diagnosis of cardiac amyloidosis. JACC: Cardiovascular Imaging. 2013;6(4).
26. Kellman P, Bandettini WP, Mancini C, Hammer-Hansen S, Hansen MS, Arai AE. Characterization of myocardial T1-mapping bias caused by intramyocardial fat in inversion recovery and saturation recovery techniques. Journal of Cardiovascular Magnetic Resonance. 2015 May 10;17(1).
27. Karur GR, Robison S, Iwanochko RM, Morel CF, Crean AM, Thavendiranathan P, et al. Use of myocardial T1 mapping at 3.0 T to differentiate anderson-Fabry disease from hypertrophic cardiomyopathy. Radiology. 2018;288(2).

28. Torlasco C, Cassinerio E, Roghi A, Faini A, Capecchi M, Abdel-Gadir A, et al. Role of T1 mapping as a complementary tool to T2 for non-invasive cardiac iron overload assessment. PLoS ONE. 2018 Feb 1;13(2).
29. Bulluck H, Rosmini S, Abdel-Gadir A, Bhuva AN, Treibel TA, Fontana M, et al. Diagnostic performance of T1 and T2 mapping to detect intramyocardial hemorrhage in reperfused ST-segment elevation myocardial infarction (STEMI) patients. Journal of Magnetic Resonance Imaging. 2017;46(3).
30. Swoboda PP, McDiarmid AK, Erhayiem B, Broadbent DA, Dobson LE, Garg P, et al. Assessing Myocardial Extracellular Volume by T1 Mapping to Distinguish Hypertrophic Cardiomyopathy from Athlete's Heart. Vol. 67, Journal of the American College of Cardiology. Elsevier USA; 2016. p. 2189–90.
31. Zhang Y, Yeung HN, O'Donnell M, Carson PL. Determination of Sample Time for T1 Measurement. Journal of Medical Resonance Imaging. 1998;8(3):675–81.
32. Dabir D, Child N, Kalra A, Rogers T, Gebker R, Jabbour A, et al. Reference values for healthy human myocardium using a T1 mapping methodology: results from the International T1 Multicenter cardiovascular magnetic resonance study. J Cardiovasc Magn Reson. 2014;16.
33. Pykett IL, Rosen BR, Buonanno FS, Brady TJ. Measurement of spin-lattice relaxation times in nuclear magnetic resonance imaging. Physics in Medicine and Biology. 1983;28(6).
34. Piechnik SK, Ferreira VM, Dall'Armellina E, Cochlin LE, Greiser A, Neubauer S, et al. Shortened Modified Look-Locker Inversion recovery (ShMOLLI) for clinical myocardial T1-mapping at 1.5 and 3 T within a 9 heartbeat breathhold. Journal of Cardiovascular Magnetic Resonance [Internet]. 2010 Nov 19 [cited 2022 May 29];12(1):1–11. Available from: https://jcmr-online.biomedcentral.com/articles/10.1186/1532-429X-12-69
35. Weingärtner S, Akcakaya M, Berg S, Kissinger K v, Manning WJ, Nezafat R. Heart-rate independent myocardial T1-mapping using combined saturation and inversion preparation pulses. Journal of Cardiovascular Magnetic Resonance [Internet]. 2013 Jan [cited 2022 May 29];15(Suppl 1):P46. Available from: /pmc/articles/PMC3559995/
36. Chow K, Flewitt JA, Green JD, Pagano JJ, Friedrich MG, Thompson RB. Saturation recovery single-shot acquisition (SASHA) for myocardial T(1) mapping. Magn Reson Med [Internet]. 2014 [cited 2022 May 29];71(6):2082–95. Available from: https://pubmed.ncbi.nlm.nih.gov/23881866/
37. Haaf P, Garg P, Messroghli DR, Broadbent DA, Greenwood JP, Plein S. Cardiac T1 Mapping and Extracellular Volume (ECV) in clinical practice: A comprehensive review. Journal of Cardiovascular Magnetic Resonance [Internet]. 2016 Nov 30 [cited 2022 May 29];18(1):1–12. Available from: https://jcmr-online.biomedcentral.com/articles/10.1186/s12968-016-0308-4
38. Look DC, Locker DR. Time saving in measurement of NMR and EPR relaxation times. Review of Scientific Instruments. 1970;41(2):250–1.
39. Graumann R, Barfuss H, Fischer H, Hentschel D, Oppelt A. TOMROP: eine Sequenz zur Bestimmung der Laengsrelaxationszeit T1 in der Kernspintomographie. Electromedica. 1987;55(2):67–72.
40. Karlsson M, Nordell B. Phantom and in vivo study of the Look–Locker T1 mapping method. Magnetic Resonance Imaging. 1999 Dec 1;17(10):1481–8.
41. Henderson E, McKinnon G, Lee TY, Rutt BK. A fast 3D Look-Locker method for volumetric T1 mapping. Magnetic Resonance Imaging. 1999;17(8).

42. Freeman AJ, Gowland PA, Mansfield P. Optimization of the ultrafast look-locker echo-planar imaging T1 mapping sequence. Magnetic Resonance Imaging. 1998;16(7).
43. Brix G, Schad LR, Deimling M, Lorenz WJ. Fast and precise T1 imaging using a TOMROP sequence. Magnetic Resonance Imaging. 1990;8(4).
44. Wacker CM, Bock M, Hartlep AW, Beck G, van Kaick G, Ertl G, et al. Changes in myocardial oxygenation and perfusion under pharmacological stress with dipyridamole: Assessment using T2* and T1 measurements. Magnetic Resonance in Medicine. 1999;41(4).
45. Cui Y, Chen Y, Cao Y, Liu J, Song J, Zhang S, et al. Myocardial extracellular volume fraction measurements with MOLLI 5(3)3 by cardiovascular MRI for the discrimination of healthy volunteers from dilated and hypertrophic cardiomyopathy patients CONCLUSION: The increased ECV in DCM and HCM patients reflects myocardial extracellular matrix expansion. Myocardial ECV provides good diagnostic performance for identifying DCM and HCM patients from healthy volunteers. [cited 2022 May 25]; Available from: https://doi.org/10.1016/j.crad.2019.04.019
46. Scheffler K, Hennig J. T1 quantification with inversion recovery TrueFISP. Magn Reson Med [Internet]. 2001 [cited 2022 May 24];45(4):720–3. Available from: https://pubmed.ncbi.nlm.nih.gov/11284003/
47. Pruessmann KP, Weiger M, Scheidegger MB, Boesiger P. SENSE: Sensitivity encoding for fast MRI. Magnetic Resonance in Medicine. 1999;42(5).
48. Liu S, Bustin A, Burshka D, Menini A, Odille F. GPU implementation of levenberg-marquardt optimization for T1 mapping. In: Computing in Cardiology. IEEE Computer Society; 2017. p. 1–4.
49. Blamire AM. The technology of MRI — the next 10 years? http://dx.doi.org/101259/bjr/96872829 [Internet]. 2014 Jan 28 [cited 2022 Jun 11];81(968):601–17. Available from: https://www.birpublications.org/doi/10.1259/bjr/96872829
50. Hwan Jin K, McCann MT, Froustey E, Unser M. Deep Convolutional Neural Network for Inverse Problems in Imaging. IEEE TRANSACTIONS ON IMAGE PROCESSING [Internet]. 2017;26(9):4509. Available from: http://www.ieee.org/publications_standards/publications/rights/index.html
51. Marty B, Vignaud A, Greiser A, Robert B, de Sousa PL, Carlier PG. Bloch equations-based reconstruction of myocardium T1 maps from modified look-locker inversion recovery sequence. PLoS ONE. 2015 May 11;10(5):329–36.
52. Lee JJ, Liu S, Nacif MS, Ugander M, Han J, Kawel N, et al. Myocardial T1 and extracellular volume fraction mapping at 3 Tesla. Journal of Cardiovascular Magnetic Resonance. 2011;13(1).
53. Shao J, Rapacchi S, Nguyen KL, Hu P. Myocardial T1 mapping at 3.0 tesla using an inversion recovery spoiled gradient echo readout and bloch equation simulation with slice profile correction (BLESSPC) T1 estimation algorithm. Journal of Magnetic Resonance Imaging [Internet]. 2016 Feb 1 [cited 2022 Jun 12];43(2):414–25. Available from: https://onlinelibrary.wiley.com/doi/full/10.1002/jmri.24999
54. Sussman MS, Yang IY, Fok KH, Wintersperger BJ. Inversion group (IG) fitting: A new T1 mapping method for modified look-locker inversion recovery (MOLLI) that allows arbitrary inversion groupings and rest periods (including no rest period). Magnetic Resonance in Medicine [Internet]. 2016 Jun 1 [cited 2022

Jun 12];75(6):2332–40. Available from: https://onlinelibrary.wiley.com/doi/full/10.1002/mrm.25829
55. Shao J, Nguyen KL, Natsuaki Y, Spottiswoode B, Hu P. Instantaneous signal loss simulation (InSiL): An improved algorithm for myocardial T1 mapping using the MOLLI sequence. Journal of Magnetic Resonance Imaging [Internet]. 2015 Mar 1 [cited 2022 Jun 12];41(3):721–9. Available from: https://onlinelibrary.wiley.com/doi/full/10.1002/jmri.24599
56. Kellman P, Herzka DA, Hansen MS. Adiabatic inversion pulses for myocardial T1 mapping. Magnetic Resonance in Medicine [Internet]. 2014 Apr 1 [cited 2022 Jun 12];71(4):1428–34. Available from: https://onlinelibrary.wiley.com/doi/full/10.1002/mrm.24793
57. Gai ND, Stehning C, Nacif M, Bluemke DA. Modified Look-Locker T1 evaluation using Bloch simulations: Human and phantom validation. Magnetic Resonance in Medicine. 2013;69(2):329–36.
58. Azlan CA, Giovanni P di, Ahearn TS, Semple SIK, Gilbert FJ, Redpath TW. B1 Transmission-Field Inhomogeneity and Enhancement Ratio Errors in Dynamic Contrast-Enhanced MRI (DCE-MRI) of the Breast at 3T. J Magn Reson Imaging [Internet]. 2010;31:234–9. Available from: www.interscience.wiley.com
59. Yarnykh VL. Actual flip-angle imaging in the pulsed steady state: a method for rapid three-dimensional mapping of the transmitted radiofrequency field. Magn Reson Med [Internet]. 2007 [cited 2022 May 29];57(1):192–200. Available from: https://pubmed.ncbi.nlm.nih.gov/17191242/
60. Ibrahim TS, Robert L, Abduljalil AM, Baertlein BA, Robitaille PML. Dielectric resonances and B(1) field inhomogeneity in UHFMRI: computational analysis and experimental findings. Magn Reson Imaging [Internet]. 2001 [cited 2022 May 29];19(2):219–26. Available from: https://pubmed.ncbi.nlm.nih.gov/11358660/
61. Poggio T, Mhaskar H, Rosasco L, Miranda B, Liao Q. Why and when can deep-but not shallow-networks avoid the curse of dimensionality: A review. International Journal of Automation and Computing. 2017 Oct 1;14(5):503–19.
62. Rosenblatt F. The Perceptron: A probabilistic model for information storage and organization in the brain. Psychological Review. 1955;65(6):386–408.
63. Mitchell TM. Machine Learning. McGraw-Hill Science/Engineering/Math; 1997. 2 p.
64. Rumelhart DE, Hinton GE, Williams RJ. Learning representations by back-propagating errors. Nature 1986 323:6088 [Internet]. 1986 [cited 2022 Jun 14];323(6088):533–6. Available from: https://www.nature.com/articles/323533a0
65. What are Convolutional Neural Networks? | IBM [Internet]. [cited 2022 Jun 14]. Available from: https://www.ibm.com/cloud/learn/convolutional-neural-networks
66. Mouton C, Myburgh JC, Davel MH. Stride and Translation Invariance in CNNs. Communications in Computer and Information Science [Internet]. 2020 [cited 2022 Jun 14];1342:267–81. Available from: https://link.springer.com/chapter/10.1007/978-3-030-66151-9_17
67. Krizhevsky A, Sutskever I, Hinton GE. ImageNet Classification with Deep Convolutional Neural Networks. [cited 2022 Jun 14]; Available from: http://code.google.com/p/cuda-convnet/
68. Esteva A, Kuprel B, Novoa RA, Ko J, Swetter SM, Blau HM, et al. Dermatologist-level classification of skin cancer with deep neural networks. Nature 2017 542:7639 [Internet]. 2017 Jan 25 [cited 2022 May

25];542(7639):115–8. Available from: https://www.nature.com/articles/nature21056
69. Liu Y, Gadepalli K, Norouzi M, Dahl GE, Kohlberger T, Boyko A, et al. Detecting Cancer Metastases on Gigapixel Pathology Images.
70. Dawes TJW, de Marvao A, Shi W, Fletcher T, Watson GMJ, Wharton J, et al. Machine learning of threedimensional right ventricular motion enables outcome prediction in pulmonary hypertension: A cardiac MR imaging study. Radiology [Internet]. 2017 May 1 [cited 2022 May 25];283(2):381–90. Available from: https://pubs.rsna.org/doi/full/10.1148/radiol.2016161315
71. Chen JF, Chen WL, Huang CP, Huang SH, Chen AP. Financial time-series data analysis using deep convolutional neural networks. Proceedings - 2016 7th International Conference on Cloud Computing and Big Data, CCBD 2016. 2017 Jul 13;87–92.
72. Shao J, Ghodrati V, Nguyen KL, Hu P. Fast and accurate calculation of myocardial T1 and T2 values using deep learning Bloch equation simulations (DeepBLESS). Magnetic Resonance in Medicine. 2020 Nov 1;84(5):2831–45.
73. Shao J, Liu D, Sung K, Nguyen KL, Hu P. Accuracy, precision, and reproducibility of myocardial T1 mapping: A comparison of four T1 estimation algorithms for modified look-locker inversion recovery (MOLLI). Magnetic Resonance in Medicine [Internet]. 2017 Nov 1 [cited 2022 Jun 11];78(5):1746–56. Available from: https://onlinelibrary.wiley.com/doi/full/10.1002/mrm.26565
74. Iglesias MA, Camara O, Sitges M, Delso G. Spatially constrained Deep Learning approach for myocardial T1 mapping. Functional Imaging and Modelling of the Heart. 2021;148–58.
75. van Gelderen P, de Zwart JA, Starewicz P, Hinks RS, Duyn JH. Real-time shimming to compensate for respiration-induced B0 fluctuations. Magnetic Resonance in Medicine [Internet]. 2007 Feb 1 [cited 2022 Jun 11];57(2):362–8. Available from: https://onlinelibrary.wiley.com/doi/full/10.1002/mrm.21136
76. Stockmann JP, Wald LL. In vivo B0 field shimming methods for MRI at 7 T. Neuroimage. 2018 Mar 1;168:71–87.
77. Messroghli DR, Greiser A, Fröhlich M, Dietz R, Schulz-Menger J. Optimization and validation of a fully-integrated pulse sequence for modified look-locker inversion-recovery (MOLLI) T1 mapping of the heart. Journal of Magnetic Resonance Imaging [Internet]. 2007 Oct 1 [cited 2022 Jun 12];26(4):1081–6. Available from: https://onlinelibrary.wiley.com/doi/full/10.1002/jmri.21119
78. Ronneberger O, Fischer P, Brox T. U-Net: Convolutional Networks for Biomedical Image Segmentation. Lecture Notes in Computer Science (including subseries Lecture Notes in Artificial Intelligence and Lecture Notes in Bioinformatics) [Internet]. 2015 [cited 2022 May 25];9351:234–41. Available from: https://link.springer.com/chapter/10.1007/978-3-319-24574-4_28
79. Levenberg K. A Method for the Solution of certain Non-Linear Problems in Least Squares. Quarterly of Applied Mathematics. 1944;2:164–8.
80. A Gentle Introduction to the Rectified Linear Unit (ReLU) [Internet]. [cited 2022 May 25]. Available from: https://machinelearningmastery.com/rectified-linear-activation-function-for-deep-learning-neural-networks/
81. Understanding the 3 most common loss functions for Machine Learning Regression | by George Seif | Towards Data Science [Internet]. [cited 2022 May 29]. Available from: https://towardsdatascience.com/understanding-the-3-most-common-loss-functions-for-machine-learning-regression-23e0ef3e14d3

82. Kingma DP, Ba JL. Adam: A Method for Stochastic Optimization. 3rd International Conference on Learning Representations, ICLR 2015 - Conference Track Proceedings [Internet]. 2014 Dec 22 [cited 2022 May 29]; Available from: https://arxiv.org/abs/1412.6980v9
83. Sacolick LI, Wiesinger F, Hancu I, Vogel MW. B1 Mapping by Bloch-Siegert Shift. Magnetic resonance in medicine : official journal of the Society of Magnetic Resonance in Medicine / Society of Magnetic Resonance in Medicine [Internet]. 2010 [cited 2022 Jun 14];63(5):1315. Available from: /pmc/articles/PMC2933656/
84. Kim S, Jang H, Hong S, Hong YS, Bae WC, Kim S, et al. Fat-saturated image generation from multi-contrast MRIs using generative adversarial networks with Bloch equation-based autoencoder regularization. Medical Image Analysis. 2021 Oct 1;73.
85. Glossary of MRI Terms. American College of Radiology;

SUPPORTING INFORMATION

- **1st section**

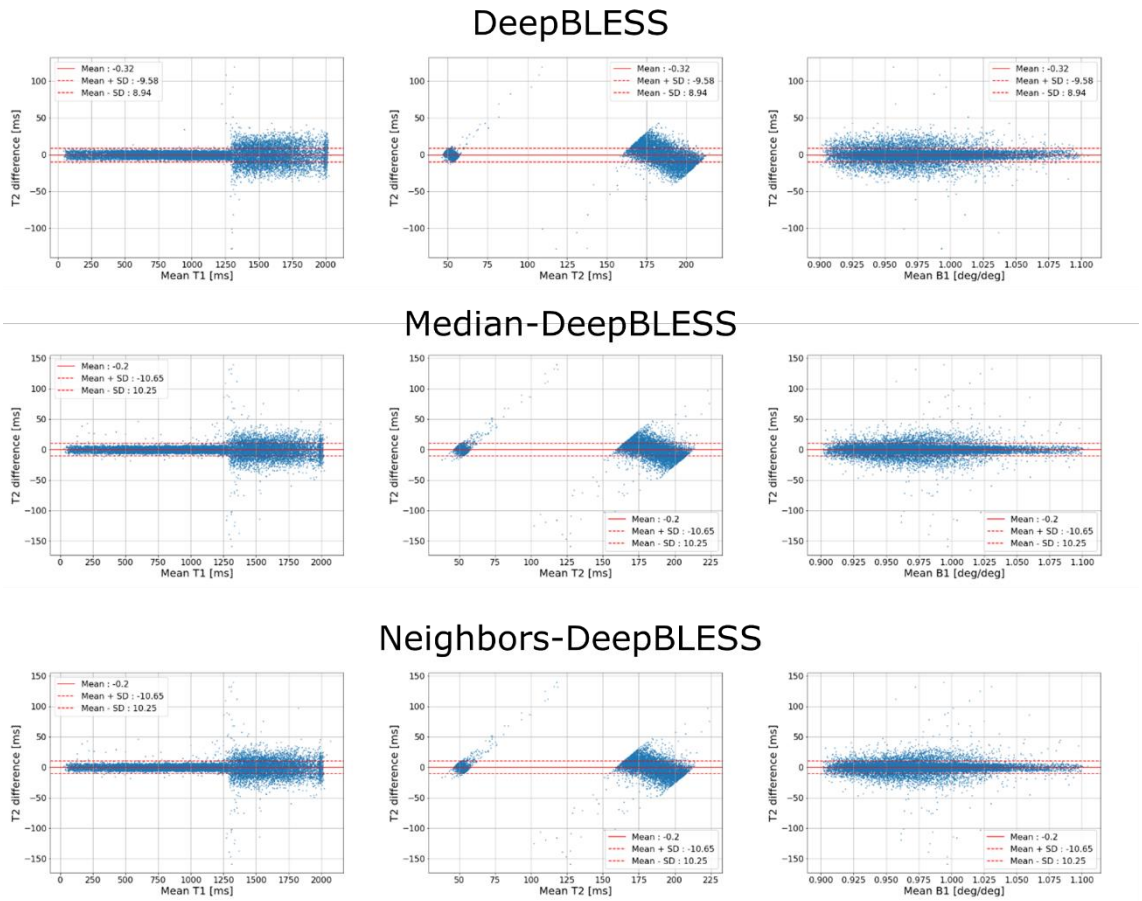

Figure 18: Bland Altman plots of the T2 estimation error with relation to the mean value of each parameter (T1, T2, and B1).

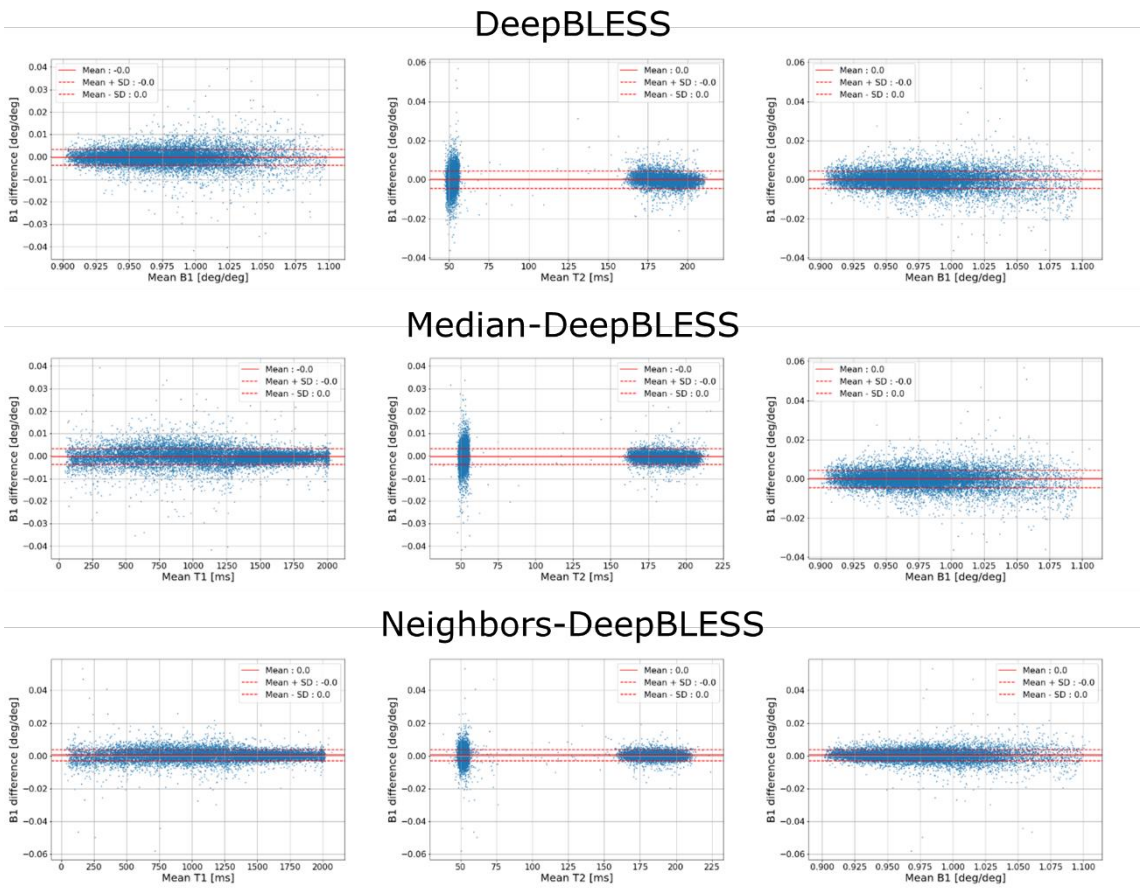

Figure 19: Bland Altman plots of the B1 estimation error with relation to the mean value of each parameter (T1, T2, and B1).

ALPHABETICAL INDEX

The following definitions have been extracted from the *Glossary of MRI terms* of the *American College of Radiology* (85).

Bo: A conventional symbol for the constant magnetic (induction) field in an MR system. (Although historically used, Ho (units of magnetic field strength, ampere/meter) should be distinguished from the more appropriate Bo [units of magnetic induction, tesla]).

B1: A conventional symbol for the radiofrequency magnetic induction field used in an MR system (another symbol historically used is H1). It is useful to consider it as composed of two oppositely rotating vectors, usually in a plane transverse to Bo. At the Larmor frequency, the vector rotating in the same direction as the precessing spins will interact strongly with the spins.

Balanced steady-state free precession: An MR gradient echo pulse sequence designed to produce contrast weighted by the T2/T1 ratio, with higher SNR and reduced artifacts compared to SSFP. Typically, TR is set to be as short as possible (short compared to the T2 values of the tissues of interest), TE is intermediate (approximately TR/2), and a flip angle of 45o to 90o is used to result in T2/T1-weighted SSFP images. Balanced SSFP sequences use specific "balanced" gradients to return the magnetization to the same phase it had before the gradients were applied, thus increasing signal and reducing artifacts. Specific vendor names for this sequence include True-Flash imaging with steady-state precession (True-FISP), fast imaging employing steady-state acquisition (FIESTA), and balanced fast-field echo (balanced-FFE). See Steady-state free precession.

Birdcage coil: An RF volume coil designed to produce a homogeneous B1 field by using multiple parallel conductors symmetrically spaced around the surface of a cylinder, connected by end rings. These are turned into low pass or high pass filter sections by adding capacitors in each conductor, or between each conductor, in the end, rings, so that at resonance there is a resulting homogeneous B1 field. When the B1 field is circularly polarized, the structure can be used as a quadrature coil.

Bloch equations: Phenomenological "classical" equations of motion for the macroscopic magnetization vector. They include the effects of precession about the magnetic field (static and RF) and the T1 and T2 relaxation times.

Coil: Single or multiple loops of wire (or another electrical conductor, such as tubing, etc.) designed either to produce a magnetic field from current flowing through the wire or to detect a changing magnetic field by voltage induced in the wire.

Contrast: In conventional radiography, contrast is defined as the difference in the signal intensities divided by the average signal intensity in two adjacent regions. In a general sense, we can consider image contrast, where the strength of the image intensity in adjacent regions of the image is compared, or object contrast, where the relative values of a parameter affecting the image (such as spin density or relaxation time) in corresponding adjacent regions of the object are compared. Relating image contrast to object contrast is more difficult in MR imaging than in conventional radiography, as there are more object parameters affecting the image and their relative contributions are very dependent on the particular imaging technique used. As in other kinds of imaging, image

contrast in MRI will also depend on region size, as reflected through the modulation transfer function (MTF) characteristics. The contrast between an object (e.g., lesion) and the background will also depend on the particular choice of designated background (e.g., fat, muscle, etc.). Contrast agent. Substance administered to the subject being imaged to alter selectively the image intensity of a particular anatomical or functional region, typically by altering the relaxation times, including T1, T2, and T2*.

Dephasing: The loss of magnetization in the transverse plane, typically due to the fact that different magnetic dipoles of different nuclei are precessing about the main magnetic field, Bo, at slightly different precessional frequencies and therefore lose phase coherence.

Dynamic range: Range of signal intensities that may need to be distinguished in an image or spectrum or that can be distinguished by the electronic components. If the signal dynamic range is too great, the need to keep the highest intensities from overloading the digitizer may result in the weaker features being lost in the digitization noise. This can be dealt with by using an analog to digital converter with a larger range of sensitivity or by using techniques to reduce the dynamic range, e.g., suppressing the signal from water in order to detect the signal from less abundant compounds.

Echo Time (TE): Time between the middle of exciting (e.g., 90°) RF pulse and the middle of spin-echo production. For multiple echos, use TE1, TE2, etc. When the RF spin-echo and gradient-echo are not coincident in time, TE refers to the time of the gradient spin echo.

Gadolinium: Lanthanide element that is paramagnetic in its trivalent state. It has been used as the active component of most contrast agents in MR imaging because of its effect of strongly decreasing the T1 relaxation times of the tissues to which it has access. Although toxic by itself, it can be given safely in a chelated form such as Gd-DTPA, which still retains much of its strong effect on relaxation times.

Gating: Synchronization of imaging with a phase of the cardiac or respiratory cycles. A variety of means for detecting these cycles can be used, such as the ECG, peripheral pulse, chest motion, etc. The synchronization can be prospective or retrospective.

Gradient-Echo: A signal echo produced by reversing the direction of a magnetic field gradient or by applying balanced pulses of magnetic field gradient before and after a refocusing RF pulse so as to cancel out the position-dependent phase shifts that have accumulated due to the gradient. In the latter case, the gradient echo is generally adjusted to be coincident with the RF spin echo. When the RF and gradient echoes are not coincident, the time of the gradient echo is denoted TE and the difference in time between the echoes is denoted TD, while TER refers to the time of the RF spin echo.

Inversion: A nonequilibrium state in which the net magnetization vector is oriented opposite to the magnetic field; usually produced by adiabatic fast passage or 180° RF pulses.

Inversion-recovery (IR): Pulsed MR imaging sequence wherein the nuclear magnetization is inverted at a time on the order of T1 before the regular imaging pulse-gradient sequences. The resulting partial relaxation of the spins in the different structures

being imaged can be used to produce an image that depends strongly on T1. This may bring out differences in the appearance of structures with different T1 relaxation times. Note that this does not directly produce an image of T1. T1 in a given region can be calculated from the change in the NMR signal from the region due to the inversion pulse compared to the signal with no inversion pulse or an inversion pulse with a different inversion time (TI).

Inversion time (TI): In inversion recovery, the time between the middle of inverting (180°) RF pulse and the middle of the subsequent exciting (90°) pulse to detect the amount of longitudinal magnetization.

Larmor frequency (ωo or fo): The frequency at which magnetic resonance can be excited; given by the Larmor equation. By varying the magnetic field across the body with a magnetic field gradient, the corresponding variation of the Larmor frequency can be used to encode position. For protons (hydrogen nuclei), the Larmor frequency is 42.58 MHz/tesla.

Lattice: By analogy to NMR in solids, the magnetic and thermal environment with which nuclei exchange energy in longitudinal relaxation.

Net magnetization vector (NMV or M): Net magnetic moment per unit volume (a vector quantity) of a sample in a given region, considered as the integrated effect of all the individual microscopic nuclear magnetic moments.

Nutation: A displacement of the axis of a spinning body away from the simple cone-shaped figure which would be traced by the axis during precession. In the rotating frame of reference, the nutation caused by an RF pulse appears as a simple precession, although the motion is more complex in the stationary frame of reference.

Off-resonance factor (Δf): A state occurring when the Larmor frequency of a spin isochromat is different from that of the exciting RF field.

Pixel: Acronym for a picture element; the smallest discrete part of a digital image display. Note that the corresponding size of the pixel may be smaller than the actual spatial resolution.

Precession: Comparatively slow gyration of the axis of a spinning body so as to trace out a cone; caused by the application of a torque tending to change the direction of the rotation axis, and continuously directed at right angles to the plane of the torque. The magnetic moment of a nucleus with spin will experience such a torque when inclined at an angle to the magnetic field, resulting in precession at the Larmor frequency. Familiar examples are the effect of gravity on the motion of a spinning top, gyroscope, or the rotating earth.

Pulse sequences: Set of RF (and/or gradient) magnetic field pulses and time spacings between these pulses; used in conjunction with magnetic field gradients and MR signal reception to produce MR images. See also Interpulse times. A recommended shorthand designation of interpulse times used to generate a particular image is to list the repetition time (TR), the echo time (TE), and, if using inversion-recovery, the inversion time, TI, with all times given in milliseconds. For example, 2500/30/1000 would indicate an inversion-recovery pulse sequence with TR of 2500 msec, TE of 30 msec, and TI of 1000

msec. If using multiple spin echoes, as in CPMG, the number of the spin-echo used should be stated.

Radiofrequency (RF): Wave frequency intermediate between auditory and infrared. The RF used in MR studies is commonly in the megahertz (MHz) range. The RF used in ESR studies is commonly in the gigahertz (GHz) range. The principal effect of RF magnetic fields on the body is power deposition in the form of heating, mainly at the surface; this is a principal area of concern for safety limits.

Random noise: Noise whose amplitude follows some probability distribution and is uncorrelated.

Region-of-interest (ROI): A user-defined subset of pixels in a planar image.

Repetition Time (TR): The period of time between the beginning of a pulse sequence and the beginning of the succeeding (essentially identical) pulse sequence.

Resonance: A large amplitude vibration in a mechanical or electrical system caused by a relatively small periodic stimulus with a frequency at or close to a natural frequency of the system; in MR apparatus, resonance can refer to the NMR itself or to the tuning of the RF circuitry.

Rotating frame of reference: A frame of reference (with corresponding coordinate systems) that is rotating about the axis of the static magnetic field Bo (with respect to a stationary ("laboratory") frame of reference) at a frequency equal to that of the applied RF magnetic field, B1. Although B1 is a rotating vector, it appears stationary in the rotating frame, leading to simpler mathematical formulations.

Saturation: A nonequilibrium state in MR, in which equal numbers of spins are aligned against and with the magnetic field, so that there is no net magnetization. Can be produced by repeatedly applying RF pulses at the Larmor frequency with interpulse times short compared to T1.

Saturation recovery (SR): A particular type of partial saturation pulse sequence in which the preceding pulses leave the spins in a state of saturation so that recovery at the time of the next pulse has taken place from an initial condition of no magnetization.

Shimming: Correction of inhomogeneity of the magnetic field produced or the radiofrequency induced magnetic field of an MR system due to imperfections in the magnet or to the presence of external ferromagnetic objects. May involve changing the configuration of the magnet or the addition of shim coils (active shimming) or small pieces of steel (passive shimming).

Signal-to-noise ratio (SNR or S/N): Used to describe the relative contributions to a detected signal of the true signal and random superimposed signals ("noise"). One common method to improve (increase) the SNR is to average several measurements of the signal with the expectation that random contributions will tend to cancel out. The SNR can also be improved by sampling larger volumes (with a corresponding loss of spatial resolution) or, within limits, by increasing the strength of the magnetic field used. Surface

coils can also be used to improve local SNR. The SNR will depend, in part, on the electrical properties of the sample or patient being studied.

Slice: The effective physical extent of the "planar" region being imaged.

Spatial resolution: The smallest distance between two points in the object that can be distinguished as separate details in the image, generally indicated as a length or a number of black and white line pairs per mm. The specific criterion for the resolution to be used depends on the type of test used (e.g., bar pattern or contrast-detail phantom). As the ability to separate or detect objects depends on their contrast and the noise, and the different MR parameters of objects will affect image contrast differently for different imaging techniques, care must be taken in comparing the results of resolution phantom tests of different machines and no single simple measure of resolution can be specified. The resolution may be anisotropic. The resolution may be larger than the size corresponding to the discrete image element (pixel), although it cannot be smaller.

Spin: The intrinsic angular momentum of an elementary particle, or system of particles such as a nucleus, that is also responsible for the magnetic moment; or a particle or nucleus possessing such a spin. The spins of nuclei have characteristic fixed values. Pairs of neutrons and protons align to cancel out their spins so that nuclei with an odd number of neutrons and/or protons will have a net nonzero rotational component characterized by an integer or half-integer quantum "nuclear spin number" (I).

Tesla (T): The preferred (SI) unit of magnetic flux density. One tesla is equal to 10,000 gauss, the older (CGS) unit.

Triggering: Generation of an electrical pulse, upon detection of a physiological signal, that can be used to initiate a synchronized data-acquisition pulse sequence.